An Underwater Simultaneous Wireless Power and Data Transfer System for AUV With High-Rate Full-Duplex Communication

Yijie Wang, *Senior Member, IEEE*, Tao Li, *Graduate Student Member, IEEE*, Ming Zeng, Jianwei Mai, *Student Member, IEEE*, Peng Gu, *Graduate Student Member, IEEE*, and Dianguo Xu, *Fellow, IEEE*

***Abstract*—This article proposed an underwater simultaneous wireless power transfer and data transfer system for the autonomous underwater vehicle. The double-sided *LLCC* compensation topology is proposed to effectively suppress the interference to the data channel at switching instant. With the increase of the size and turns of the coupling coils, the self-resonance frequency gradually decreases. However, the frequency of data carriers is usually much lower than the self-resonant frequency, which will reduce the data rate or improve the bit error rate at a high data rate. Moreover, the high voltage generated by coupling coils causes high voltage stress on the data channel. To deal with these two issues, the last turn of each coupling coil is used to transfer data in the proposed system. The two transceivers are, respectively, connected with the last turn of the two coupling coils, which excites the entire coils to self-resonate and generates two resonant frequencies. The two resonant frequencies are utilized to realize high-speed full-duplex communication. And the voltage stress of the data channel is effectively reduced. A 518-W full-duplex prototype is built, and the maximum data rate is 700 kb/s, which verifies the feasibility of the proposed system.**

***Index Terms*—Double-sided *LLCC* compensation topology, dull-duplex communication, self-resonant, underwater simultaneous wireless power transfer and data transfer (USWPDT).**

I. Introduction

AUTONOMOUS underwater vehicles (AUVs) have become important equipment for underwater exploration. The insufficient battery capacity of AUV is one of the critical factors of limited maneuverability. However, underwater conductive charging requires a wet plug-in connector. There are disadvantages such as short-lived, expensive, and complex maintenance [1], [2]. Wireless power transfer (WPT) technology provides a feasible method to solve the above problems, which can significantly improve the reliability of underwater charging [3], [4], [5], [6], as shown in Fig. 1. There is data interaction between AUV and charging dock, such as feedback information of secondary sensor, uploading and downloading data, etc. [7], [8], [9]. Therefore, the underwater simultaneous wireless power and data transfer (USWPDT) system has recently attracted more attention.

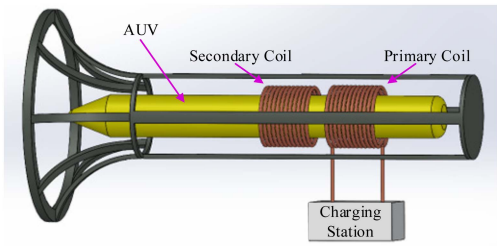

Fig. 1. Wireless power transfer for AUV.

There are many methods to achieve the simultaneous transfer of power and data. RF communication such as Bluetooth, Wi-Fi, and ZigBee have been widely used in WPT systems. These methods have the problems such as considerable pairing delay, increased size of additional modules, high bit error rate with the increase of power level, and high signal attenuation underwater [10], [11], [12]. Adding additional pairs of communication coils decoupled from the power channel can achieve high-rate data transmission [13], [14]. But the method limits the flexibility of the system design and increases the size of the system. Changing the phase and amplitude of the power waveform can also transfer data. This method has no additional components and is easy to implement, but it is challenging to realize high-rate full-duplex communication, and the load power fluctuates in the communication [15], [16], [17]. Acoustic communication can be completely decoupled from the power channel for the unique underwater environment. It is suitable for long-distance transmission and has no significant advantage at the distance of the inductive power transfer (IPT) system [18], [8]. Using the electric field to communicate underwater requires additional coupling plates, which will increase the size of the system [19].

Manuscript received 27 May 2022; revised 26 July 2022; accepted 27 August 2022. Date of publication 31 August 2022; date of current version 10 October 2022. This work was supported in part by the National Natural Science Foundation of China under Grant 51922033, in part by the Power Electronics Science and Education Development Program of Delta Group under Grant DREK2020003, and in part by the Natural Science Foundation of Heilongjiang Province under Grant YQ2020E017. Recommended for publication by Associate Editor M. Ponce-Silva. *(Corresponding author: Yijie Wang.)*

The authors are with the Harbin Institute of Technology, Harbin 150001, China (e-mail: wangyijie@hit.edu.cn; 22b306006@stu.hit.edu.cn; 21s006096@stu.hit.edu.cn; 18b906026@stu.hit.edu.cn; 614489151@qq.com; xudiang@hit.edu.cn).

Color versions of one or more figures in this article are available at https://doi.org/10.1109/TPEL.2022.3203038.

Digital Object Identifier 10.1109/TPEL.2022.3203038

The high-frequency data carriers can be loaded on the coupling coils to realize the simultaneous transmission of data and power without adding additional coils [10]. The data carrier frequency is in the megahertz frequency band, and the power channel frequency of the IPT system is usually tens of kilohertz. The two frequencies are not in the same frequency band. So this method can realize high-rate communication and is suitable for underwater WPT systems.

In [20], [21], and [22], the high-frequency data carriers are loaded on the coupling coils through transformers or capacitors. The data channel has only one resonant frequency, and the system works in half-duplex mode. In [23], [24], [25], [26], and [27], the coupling coils form a double-resonance circuit with the components of the data channel. The system utilizes the two resonant frequencies for full-duplex communication. The trap inductances are usually added to the power channel to load the high-frequency data carriers to the coupling coils [25], [26], [27]. At least two inductors are added to the power channel of the primary and secondary sides, which will increase the size of the system and affect the power transfer efficiency (PTE) of the system. The problem was solved by using the taps of the coupling coils to inject data carriers [21], [28]. One part of the coils can transfer data, and the other can be equivalent to the trap inductor. In [29], a plug-and-play toroidal-core inductor is proposed to inject and extract the data carriers, which has little effect on the power channel.

The data channel and power channel share identical coupling coils, inevitably interfering with data transfer. Through the careful design of circuit structure and parameters, [22], [23], [24], [25], [26] significantly reduce the interference of fundamental components of the power channel to the data channel. However, most of the compensation topologies are T-type networks [30], [31], [32], [33] which have little common-mode (CM) interference suppression to the data channel. The interference caused by the switching moment in the power channel is still relatively large because the switching moment has a rich harmonic spectrum, including the frequency band where the data channel works.

The working frequency of the data channel is designed to be less than the self-resonance frequency of the coupling coils in the former SWPDT system. With the increase of coil size, its self-resonance frequency will gradually decrease [34]. When the self-resonance frequency of the coupling coils is relatively low, if the data carrier frequency is still designed to be lower than the self-resonance frequency, the data rate will be reduced.

When the IPT system works, a high voltage will be generated on the coils due to resonance. The data transceiver is directly connected to the power coil, so the data channel will have considerable voltage stress [20], [21], [22], [23], [24], [25], [26], [27], [28], improving the system cost and reducing reliability.

Generally, the realization methods of full duplex communication include frequency division duplex (FDD), time division duplex (TDD), as shown in Fig. 2. TDD means that both sides of the system use the same frequency band to communicate in time division. It emulates full-duplex communication over a half-duplex communication link. The conversion of uplink and downlink transmission requires a certain guard interval, which reduces the utilization of spectrum, as shown in Fig. 2(b).

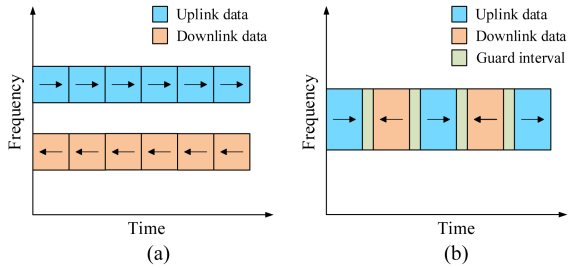

Fig. 2. FDD and TDD communication principle. (a) FDD communication principle. (b) TDD communication principle.

FDD refers to the simultaneous and independent transmission of information through multiple frequency bands in the system, as shown in Fig. 2(a). Due to the large frequency interval between channels, each frequency band will not interfere with each other after bandpass filtering, which makes it possible to transfer information in the forward and reverse directions simultaneously and independently. In addition, there is no need to add a guard interval, which improves the utilization rate of the spectrum compared with TDD and is relatively simple to control.

To further reduce the interference of the power channel to the data channel and realize a high-rate full-duplex USWPDT system, a novel topology is proposed in this article. When the transfer power is 518W and efficiency is 92%, the forward data rate is 500 kb/s, and the backward data rate is 700 kb/s. The main contributions of this study are summarized as follows.

1) The double-sided *LLCC* compensation topology is proposed to effectively suppress the interference to the data channel at switching instant. This compensation topology is almost the same size as the conventional double-sided *LCC* with limited extra loss.
2) The self-resonance of the coupling coils is used to transfer data, and the high-speed full-duplex data communication is realized under 518 W output power.
3) The voltage stress of the data channel is significantly reduced by connecting the transceivers to the last turn of the coupling coils.

II. Overview of the Proposed System

The circuit diagrams of the proposed system are shown in Fig. 3. Fig. 3(a) is the power transfer circuit and bidirectional data transfer. The power transfer channel consists of dc voltage source $U_{\rm in}$, full-bridge inverter, double-side *LLCC* compensation topology, coupling coils, rectifier, and the load. The double-side *LLCC* compensation is proposed in this article, which has the following advantages. First, it can realize load-independent output current or voltage, zero voltage switching (ZVS), and high degrees of design freedom. Second, the $L_{\rm f11}$, $L_{\rm f12}$, $C_{\rm f1}$, $L_{\rm f21}$, $L_{\rm f22,}$ and $C_{\rm f2}$ can suppress the CM and differential-mode interference generated by the full-bridge inverter and rectifier. Third, $L_{\rm f11}$ and $L_{\rm f12}$ ($L_{\rm f21}$ and $L_{\rm f22}$) are wound on the same magnetic core with a coupling coefficient above 0.9, as shown in Fig. 4, so the total size of double-side *LLCC* is almost the same as conventional double-side *LCC* compensation topology. A and B in Fig. 4(a) are connected to the output of the inverter. The

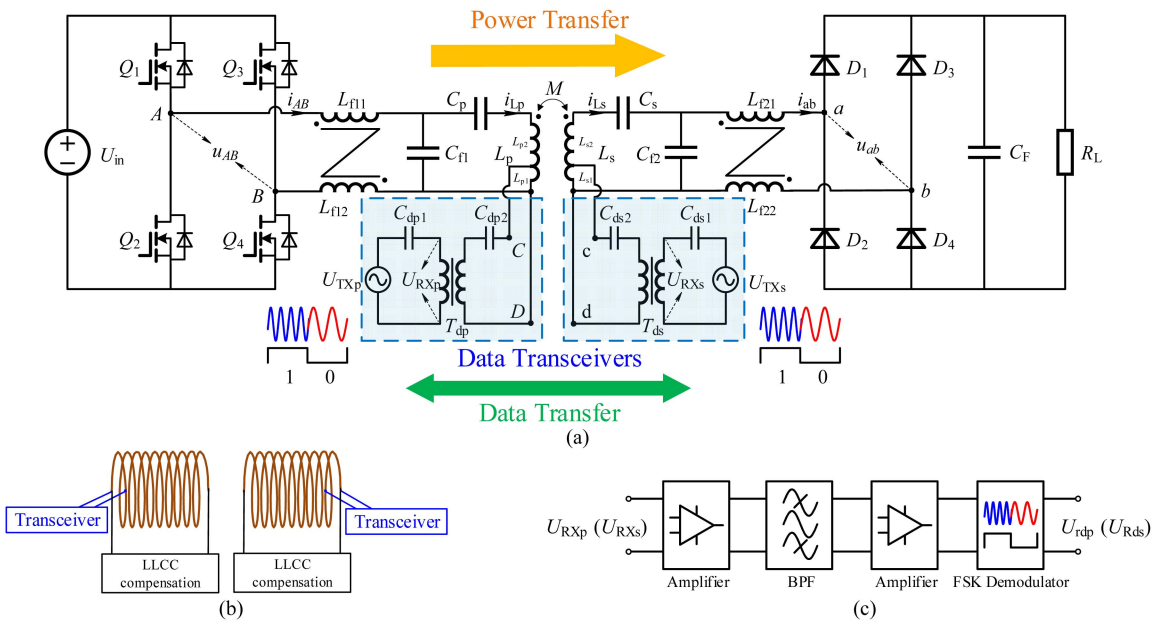

Fig. 3. Circuit diagrams of the proposed USWPDT system. (a) Power and data channel. (b) Transceivers connected to the last turn. (c) Data demodulation circuit.

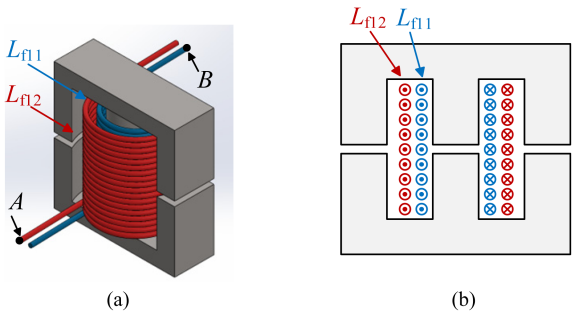

Fig. 4. Winding mode schematic diagram of L_{f11} and L_{f22}. (a) Stereogram. (b) Sectional view.

power transfer frequency is f_p. The mutual inductance of coils is M, and the load is R_L. The frequency of the power channel is 85 kHz. The Litz wire is employed to reduce the parasitic ac resistance of the transmitting and receiving coils.

The data transfer circuit in Fig. 3(a) comprises data transceivers and coupling coils. U_{TXp} (U_{TXs}) is the modulated signal on the primary (secondary) side. U_{RXp} (U_{RXs}) is the superposition of the transferred signal on the primary (secondary) side and the received signal from the secondary (primary) side. The T_{dp} and T_{ds} are signal isolation transformers that load the data carrier into the coupling coils. C_{dp1}, C_{dp2}, C_{ds1}, and C_{ds2} reduce interference generated from the power channel. The data transceiver in the primary (secondary) connects to the last turn of the transmitting (receiving) coil, as shown in Fig. 3(b). The coupling of the last turn and the entire coil makes the coil self-resonant, and the data channel generates two resonant frequencies. Take the process of transferring data from the primary side to the secondary side as an example. The primary data transceiver in this article is connected to the last turn of the primary coil, as shown in Fig. 3(b). When transmitting data, data transceiver loads the high-frequency data carrier on the last turn of the coil. The high-frequency current in the last turn generates a high-frequency magnetic field. Since the last turn of the coil is coupled to the entire coil, the magnetic field generated by the last turn excites the entire coil to resonate. The high-frequency magnetic field generated by the primary coil excites the secondary coil to resonate. Therefore, two resonance points are generated in the data channel, so that the last turn of the secondary coil will also induce a high-frequency carrier. The high-frequency carrier is sensed by the secondary transceiver and demodulated into binary data. One of the two high-frequency resonance points is used to transfer data in the forward direction, and the other is used to transfer data in the reverse direction.

According to the characteristics of the system, frequency division multiplexing (FDM) is used to realize a full duplex. There are two frequencies in the data channel of the system to make the voltage gain reach the extreme value. Therefore, the system satisfies the condition of FDM, that is, there are two frequency bands for the data channel. Due to the existence of two frequency bands in the data channel, the system has the basic conditions for FDD communication. By properly designing the bandpass filter, the mutual interference of these two frequency bands can be greatly reduced. Therefore, these two frequency bands can be used to independently forward and reverse transfer data so that the system achieves full-duplex transmission.

From the above-mentioned analysis, these two frequency bands can transfer data independently, so only the data modulation method needs to be considered. Commonly used modulation methods include phase-shift keying (PSK), frequency-shift keying (FSK), and amplitude-shift keying (ASK), as shown in Fig. 5. The principle of PSK is to distinguish 0 and 1 by detecting the difference in the phase of the received signal. The modulation and demodulation methods of phase shift keying are relatively complex. Since FSK has better antinoise and antiattenuation

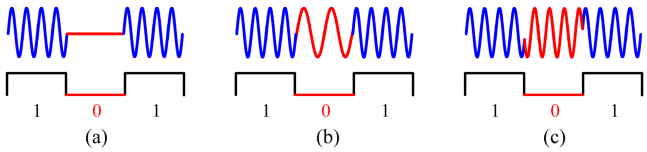

Fig. 5. Three types of modulation. (a) ASK. (b) FSK. (c) PSK.

TABLE I
MAIN PARAMETERS UTILIZED IN ANALYSIS

Symbol	Value	Symbol	Value
U_{in}	120V	L_{f1}, L_{f2}	126uH
R_L	280Ω	C_{f1}, C_{f2}	27.8nF
f_p	85kHz	C_p, C_s	11.9nF
L_{f11}, L_{f12}, L_{f21}, L_{f22}	33uH	L_p, L_s	411uH
k_{fp}, k_{fs}	0.91	L_{p1}, L_{s1}	1.1uH
C_{dp1}, C_{ds1}	220pF	M	123uH
C_{dp2}, C_{ds2}	1nF	M_{p1p2}, M_{s1s2}	8uH
L_{dpm}, L_{dsm}	7.3uH	M_{p1s1}	25nH
f_{dp}	5.4MHz	M_{p2s2}	120uH
f_{ds}	7.3MHz	M_{p1s2}, M_{p2s1}	1.7uH
R_{f1}, R_{f2}	95mΩ	R_p, R_s	500mΩ

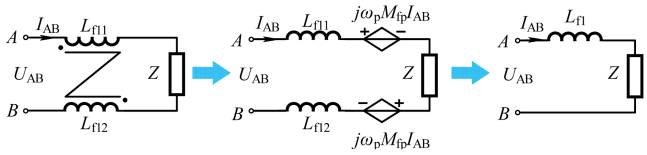

Fig. 6. Equivalent circuit of L_{f11} and L_{f12}.

capabilities than ASK [10], [22], this article selects FSK as the modulation method of data. So full-duplex data transfer can be implemented through FDM and FSK in the proposed USWPDT system.

Fig. 3(c) shows the FSK demodulation circuit. The first amplifier is to isolate the signal processing circuit from the data transceiver. The bandpass filter filters out all signals except the received signals. The filtered signal is amplified and passed through the FSK demodulator to obtain the received data. The main parameters utilized in the following analysis are listed in Table I.

III. ANALYSIS OF POWER TRANSFER CHANNEL

The dc power supply U_{in} is converted into ac voltage through the full-bridge inverter. U_{AB} is the root mean square value of the fundamental harmonic full-bridge output voltage and can be expressed as

$$U_{AB} = \frac{2\sqrt{2}}{\pi} U_{in}. \tag{1}$$

The right side of port AB can be equivalent to L_{f11} and L_{f12} in series with impedance Z, as shown in Fig. 6. Based on Kirchhoff's voltage law (KVL), U_{AB} can be expressed as

$$U_{AB} = j\omega_p L_{f11} I_{AB} + j\omega_p M_{fp} I_{AB} + j\omega_p L_{f12} I_{AB} + j\omega_p M_{fp} I_{AB} + I_{AB} Z \tag{2}$$

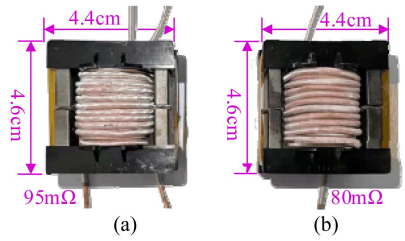

Fig. 7. Size of the new inductor and original inductor. (a) New inductor. (b) Original inductor.

where ω_p is the angular frequency of the power channel. M_{fp} is the mutual inductance of L_{f11} and L_{f12}, and $M_{fp} = k_{fp}\sqrt{L_{f11}L_{f12}}$, k_{fp} is the coupling coefficient of L_{f11} and L_{f12}.

The impedance of port AB can be obtained based on (2)

$$Z_{AB} = \frac{U_{AB}}{I_{AB}} = j\omega_p L_{f11} + j\omega_p L_{f12} + 2j\omega_p M_{fp} + Z. \tag{3}$$

The compensating inductances L_{f11} and L_{f12} can be equivalent to L_{f1}, as shown in Fig. 6. Then L_{f1} can be expressed as

$$L_{f1} = L_{f11} + L_{f12} + 2M_{fp} = L_{f11} + L_{f12} + 2k_{fp}\sqrt{L_{f11}L_{f12}}. \tag{4}$$

The compensation inductor on the secondary side is wound the same way as the primary side. Therefore, the secondary side inductors L_{f21} and L_{f22} can also be equivalent to L_{f2}. L_{f2} can be expressed as

$$L_{f2} = L_{f21} + L_{f22} + 2M_{fs} = L_{f21} + L_{f22} + 2k_{fs}\sqrt{L_{f21}L_{f22}} \tag{5}$$

where M_{fs} is the mutual inductance of L_{f21} and L_{f22}, and $M_{fs} = k_{fs}\sqrt{L_{f21}L_{f22}}$, k_{fs} is the coupling coefficient of L_{f21} and L_{f22}.

L_{f11} (L_{f21}) and L_{f12} (L_{f22}) are wound on the same core, and k_f (k_s) is larger than 0.9, so the total size of the compensation inductors is almost the same as the size of the inductor with a value of L_{f1} (L_{f2}). Taking the primary compensation inductor as an example, the size comparison is shown in Fig. 7. Their inductors are 126 μH, the equivalent series resistance (ESR) of the new inductor is 95 mΩ, and the ESR of the original inductor is 80 mΩ. The ESR of the new inductor is only slightly increased, with no change in size.

The impedance of the data transceiver port CD (cd) is

$$Z_{CD} = \frac{1}{j\omega_p C_{dp2}} + \frac{j\omega_p L_{dpm}}{1 - \omega_p^2 L_{dpm} C_{dp1}} \tag{6}$$

$$Z_{cd} = \frac{1}{j\omega_p C_{ds2}} + \frac{j\omega_p L_{dsm}}{1 - \omega_p^2 L_{dsm} C_{ds1}} \tag{7}$$

where L_{dpm} (L_{dsm}) is the coil inductance when the T_{dp} (T_{ds}) is regarded as an ideal transformer.

The following equation can be calculated by using the parameters in Table I

$$\begin{cases} |Z_{CD}| \gg |j\omega_p L_{p1}| \\ |Z_{cd}| \gg |j\omega_p L_{s1}| \end{cases}. \tag{8}$$

So the data transfer circuit has little influence on the power transfer circuit. The power transfer circuit can be simplified, as

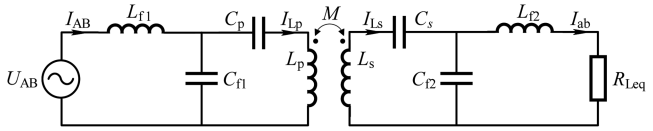

Fig. 8. Equivalent circuit of data channel. (a) Equivalent circuit. (b) Simplified equivalent circuit.

shown in Fig. 8. R_{Leq} is the equivalent load resistance of rectifier port ab, and it can be expressed as

$$R_{\mathrm{Leq}} = \frac{8}{\pi^2} R_{\mathrm{L}}. \tag{9}$$

The following equations determine the parameters of the power channel according to the classic double-sided *LCC* topology:

$$\begin{cases} \omega_{\mathrm{p}} L_{\mathrm{p}} - \frac{1}{\omega_{\mathrm{p}} C_{\mathrm{p1}}} = \frac{1}{\omega_{\mathrm{p}} C_{\mathrm{f1}}} = \omega_{\mathrm{p}} L_{\mathrm{f1}} \\ \omega_{\mathrm{p}} L_{\mathrm{s}} - \frac{1}{\omega_{\mathrm{p}} C_{\mathrm{p2}}} = \frac{1}{\omega_{\mathrm{p}} C_{\mathrm{f2}}} = \omega_{\mathrm{p}} L_{\mathrm{f2}} \end{cases}. \tag{10}$$

When the system works at the resonant frequency, the input and output current of the system and the current on the coils are expressed in the following equations [25]:

$$I_{\mathrm{AB}} = \frac{M^2 U_{\mathrm{AB}} R_{\mathrm{Leq}}}{\omega_{\mathrm{p}}^2 L_{\mathrm{p}}^2 L_{\mathrm{s}}^2} \tag{11}$$

$$I_{\mathrm{p}} = \frac{U_{\mathrm{AB}}}{j\omega_{\mathrm{p}} L_{\mathrm{p}}} \tag{12}$$

$$I_{\mathrm{s}} = \frac{M U_{\mathrm{AB}}}{\omega_{\mathrm{p}}^2 L_{\mathrm{p}} L_{\mathrm{s}}^2} \tag{13}$$

$$I_{\mathrm{ab}} = \frac{M U_{\mathrm{AB}} R_{\mathrm{Leq}}}{j\omega_{\mathrm{p}} L_{\mathrm{p}} L_{\mathrm{s}}}. \tag{14}$$

The output power and PTE can be derived as

$$P_{\mathrm{o}} = \frac{M^2 U_{\mathrm{AB}}^2 R_{\mathrm{Leq}}}{\omega_{\mathrm{p}}^2 L_{\mathrm{p}}^2 L_{\mathrm{s}}^2} \tag{15}$$

$$\eta = \frac{I_{\mathrm{ab}}^2 R_{\mathrm{Leq}}}{I_{\mathrm{AB}}^2 R_{\mathrm{f1}} + I_{\mathrm{p}}^2 R_{\mathrm{p}} + I_{\mathrm{s}}^2 R_{\mathrm{s}} + I_{\mathrm{ab}}^2 (R_{\mathrm{Leq}} + R_{\mathrm{f2}})} \tag{16}$$

where R_{f1}, R_{p}, R_{s}, and R_{f2} are the ESR of L_{f1}, L_{p}, L_{s}, and L_{f2}, respectively.

The PTE underwater is slightly lower than in the air when the frequency is low. And with the increase in frequency, the transfer characteristics of the system are more different from those in the air [7]. Therefore, the proposed system in this article selects 85 kHz as the working frequency of the system.

The fluctuation of water will lead to periodic changes in the radial misalignment and axial misalignment between the primary and secondary sides. For the power channel, normalized output current varies with the radial misalignment and axial misalignment is shown in Fig. 9. The output current of the double-side *LLCC* compensation topology is proportional to the mutual inductance. With the fluctuation of the water, the mutual inductance of the coupling coils will change periodically, so that the output current fluctuates periodically as the water fluctuates.

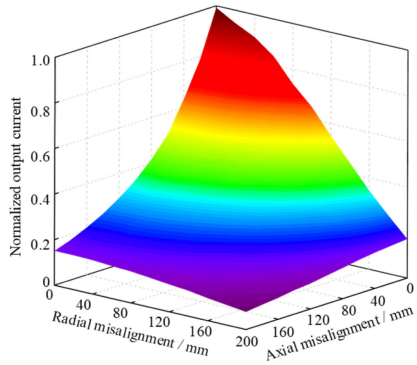

Fig. 9. Normalized output current varies with radial misalignment and axial misalignment.

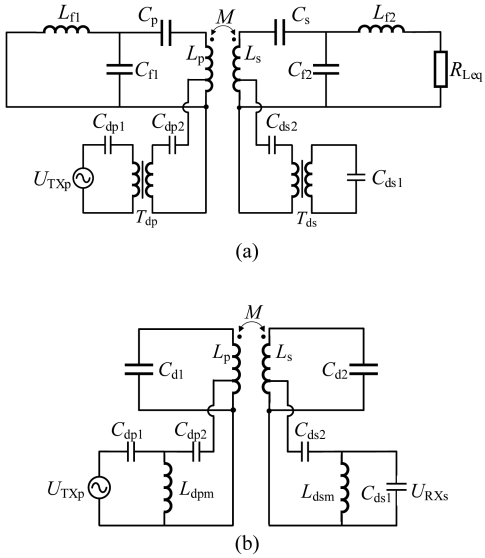

Fig. 10. Equivalent circuit of data channel. (a) Equivalent circuit. (b) Simplified equivalent circuit.

In order to stabilize the output current, a fixing device is usually added to the charging dock to fix the AUV [1]. To achieve further voltage regulation, the dc–dc converter can be cascaded after the rectifier [7] or the active rectifier technology can be used [9], but these are not the focus of this article.

IV. Analysis of Data Transfer Channel

The equivalent circuit of data transfer channel is shown in Fig. 10(a). The frequency of the data channel is f_{d} and $\omega_{\mathrm{d}} = 2\pi f_{\mathrm{d}}$. The impedance of L_{f1}, L_{f2}, C_{f1}, and C_{f2} can be expressed as

$$\begin{cases} Z_{\mathrm{Lf1}} = j\omega_{\mathrm{d}} L_{\mathrm{f1}} \\ Z_{\mathrm{Lf2}} = j\omega_{\mathrm{d}} L_{\mathrm{f2}} \\ Z_{\mathrm{Cf1}} = \frac{1}{j\omega_{\mathrm{d}} C_{\mathrm{f1}}} \\ Z_{\mathrm{Cf2}} = \frac{1}{j\omega_{\mathrm{d}} C_{\mathrm{f2}}} \end{cases}. \tag{17}$$

It can be obtained from (6) and (10)

$$\frac{|Z_{\mathrm{Lf1}}|}{|Z_{\mathrm{Cf1}}|}=\frac{|Z_{\mathrm{Lf2}}|}{|Z_{\mathrm{Cf2}}|}=\frac{\omega_{\mathrm{d}}^2}{\omega_{\mathrm{p}}^2}=\frac{f_{\mathrm{d}}^2}{f_{\mathrm{p}}^2}. \tag{18}$$

In this article, $f_{\mathrm{d}}^2/f_{\mathrm{p}}^2>3500$, thus

$$\begin{cases}|Z_{\mathrm{Lf1}}|>>|Z_{\mathrm{Cf1}}|\\ |Z_{\mathrm{Lf2}}|>>|Z_{\mathrm{Lf2}}|\end{cases}. \tag{19}$$

The compensation inductance branches can be equivalent to an open circuit. The circuit in Fig. 10(a) can be further simplified in Fig. 10(b). C_{d1} (C_{d2}) is the equivalent capacitance of C_{p} (C_{s}) and C_{f1} (C_{f2}) in series, which can be expressed as

$$\begin{cases}C_{\mathrm{d1}}=\frac{C_{\mathrm{p}}C_{\mathrm{f1}}}{C_{\mathrm{p}}+C_{\mathrm{f1}}}\\ C_{\mathrm{d2}}=\frac{C_{\mathrm{s}}C_{\mathrm{f2}}}{C_{\mathrm{s}}+C_{\mathrm{f2}}}\end{cases} \tag{20}$$

The proposed system uses the self-resonance of coils to transfer data. The inductance of the coils resonates with the parasitic capacitance between turns. At resonance, the current of each coil turn is different, and the law of current distribution on the coil at other resonance points is also different [34]. When analyzing the transfer characteristics of the coupling coils in the proposed system, the lumped-parameter mutual inductance equivalent circuit is inaccurate. Therefore, the coupling coils are equivalent to the distributed-parameter circuit model [35], as shown in Fig. 11. L_{p1}-L_{pn} (L_{s1}-L_{sn}) and R_{p1}-R_{pn} (R_{s1}-R_{sn}) are the inductance and resistance of each turn of the primary (secondary) coil. M_{pik} (M_{sik}) is the mutual inductance between any two turns of the primary (secondary) coil, where $i=1, 2, \ldots, n$, $k=1, 2, \ldots, n$, and $i\neq k$. The parasitic capacitance and its ESR between turns of the primary (secondary) coil are C_{pik} (C_{sik}) and R_{pik} (R_{sik}). The voltage of each primary (secondary) node is U_{pi} (U_{si}). The current flowing through each primary (secondary) coil turn is I_{pi} (I_{si}).

From circuit model of data channel in Fig. 12, the circuit consists of coil inductances, turn-to-turn capacitances, coil mutual inductances, and ESRs. Therefore, this article analyzes the influence of the underwater environment on the above-mentioned quantities.

The ESR of per turn can be expressed as [7]

$$R_{\mathrm{Ls}}=\omega\mu a\left[\frac{4}{3}(\beta a)^2-\frac{\pi}{3}(\beta a)^3+\frac{2\pi}{15}(\beta a)^5-\ldots\right] \tag{21}$$

where μ is the permeability of medium, a is the radius of the coil loop, $\beta=\sqrt{\mu\omega\sigma/2}$, and σ is the conductivity of water.

The self-inductance of the single-turn coil can be expressed as [36]

$$L_{\mathrm{single}}=\mu a\left(\ln\frac{8a}{b}-2\right). \tag{22}$$

The mutual inductance between two single-turn coils can be expressed as [36]

$$M_{\mathrm{single}}=\frac{\mu}{4\pi}\oint_{l_1}\oint_{l_2}\frac{d\boldsymbol{l}_1\cdot d\boldsymbol{l}_2}{|\boldsymbol{r}_{12}|} \tag{23}$$

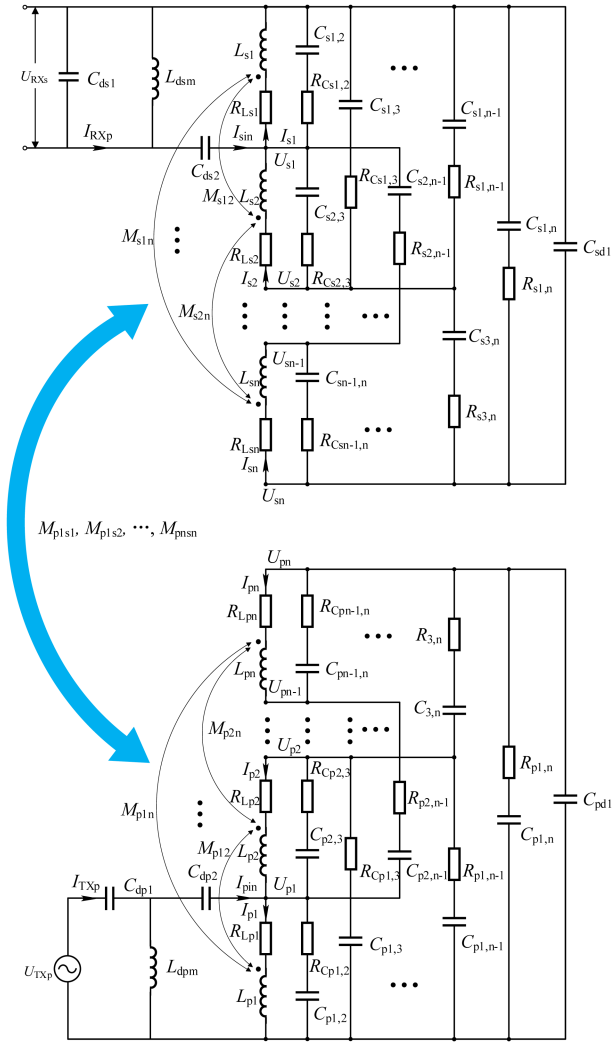

Fig. 11. Distributed-parameter circuit model of data channel.

where $d\boldsymbol{l}_1$ and $d\boldsymbol{l}_2$ are the differentials of two coils respectively. $\boldsymbol{r_{12}}$ is the vector between $d\boldsymbol{l}_1$ and $d\boldsymbol{l}_2$. μ_0 is the magnetic permeability of the vacuum.

The turn-to-turn capacitance can be expressed as [37]

$$C_{\mathrm{tt}}=\frac{2\varepsilon_0\pi D_{\mathrm{t}}}{\sqrt{\Gamma^2-1}}\cdot\tan^{-1}\left(\sqrt{1+\frac{2}{\Gamma-1}}\right) \tag{24}$$

where $\Gamma=1/\varepsilon_{\mathrm{r}}\ln(d_{\mathrm{o}}/d_{\mathrm{i}})+p/d_{\mathrm{o}}$, d_{i} and d_{o} are the inner and outer diameters of the round conductor, p is the winding pitch, ε_0 is the absolute permittivity of free space, ε_{r} is the relative permittivity of the medium.

The conductivity and relative permittivity of water are different compared to air. From (21)–(24), the ESR and turn-to-turn capacitance changed compared to the air. In this article, the values of the above-mentioned parameters in the underwater environment are obtained by the finite element simulation software Ansys HFSS and Ansys Q3D, as shown in Fig. 12.

Fig. 12(a) is the turn-to-turn capacitance varies with the distance. The turn-to-turn capacitance decreases with the increased distance, which is significantly greater in an underwater

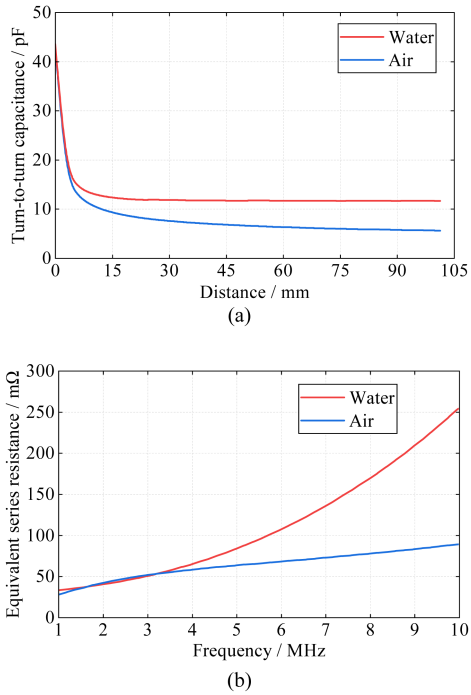

Fig. 12. Capacitance and resistance in water and air vary with distance. (a) Turn-to-turn capacitance varies with the distance. (b) ESR of one turn varies with the frequency.

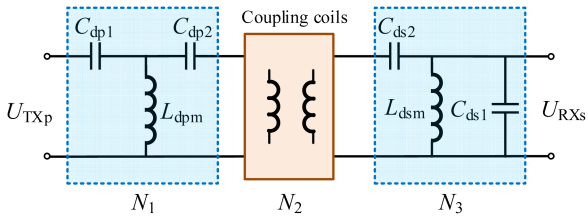

Fig. 13. Cascade of N_1, N_2, and N_3.

environment than in the air. Fig. 12(b) is the ESR of one turn varies with the frequency. The resistance of the underwater coil increases significantly with frequency compared to in the air. The values of turn-to-turn capacitance and ESR of coil under water are completely different from those in the air. Therefore, these values should be obtained in the underwater environment.

The circuit shown in Fig. 11 can be equivalent to a cascade of three two-port networks (N_1, N_2, and N_3), as shown in Fig. 13. The transmission parameters (ABCD parameters) of network N_1 and network N_3 can be obtained directly from the circuit structure, then $\boldsymbol{A}_{\mathrm{N1}}$ and $\boldsymbol{A}_{\mathrm{N3}}$ can be expressed as

$$\boldsymbol{A}_{\mathrm{N1}} = \begin{bmatrix} A' & B' \\ C' & D' \end{bmatrix} = \begin{bmatrix} 1+\frac{Z'_{\mathrm{A}}}{Z'_{\mathrm{C}}} & Z'_{\mathrm{A}}+Z'_{\mathrm{B}}+\frac{Z'_{\mathrm{A}}Z'_{\mathrm{B}}}{Z'_{\mathrm{C}}} \\ \frac{1}{Z'_{\mathrm{C}}} & 1+\frac{Z'_{\mathrm{B}}}{Z'_{\mathrm{C}}} \end{bmatrix} \tag{25}$$

$$\boldsymbol{A}_{\mathrm{N3}} = \begin{bmatrix} A''' & B''' \\ C''' & D''' \end{bmatrix} = \begin{bmatrix} 1+\frac{Z'''_{\mathrm{A}}}{Z'''_{\mathrm{C}}} & Z'''_{\mathrm{A}}+\frac{Z'''_{\mathrm{A}}}{Z'''_{\mathrm{C}}} \\ \frac{1}{Z'''_{\mathrm{C}}} & 1 \end{bmatrix} \tag{26}$$

where

$$Z'_{\mathrm{A}} = \frac{1}{sC_{\mathrm{dp1}}},\ Z'_{\mathrm{B}} = \frac{1}{sC_{\mathrm{dp2}}}, Z'_{\mathrm{C}} = sL_{\mathrm{dpm}},\ Z'''_{\mathrm{A}} = \frac{1}{sC_{\mathrm{ds2}}},$$

$$Z'''_{\mathrm{C}} = \frac{sL_{\mathrm{dsm}}}{1+s^2L_{\mathrm{dsm}}C_{\mathrm{ds1}}},\ s = j\omega_{\mathrm{d}}.$$

According to KVL and KCL, the following equations can be obtained from the circuit in Fig. 11

$$\begin{cases} \boldsymbol{Y}_{\mathrm{C1}}\boldsymbol{U}_{\mathrm{p}} + \boldsymbol{B}\boldsymbol{I}_{\mathrm{p}} = \boldsymbol{I}_{\mathrm{pin}} \\ \boldsymbol{A}\boldsymbol{U}_{\mathrm{p}} = \boldsymbol{Z}_{\mathrm{p}}\boldsymbol{I}_{\mathrm{p}} + s\boldsymbol{M}_{\mathrm{p}}\boldsymbol{I}_{\mathrm{p}} + s\boldsymbol{M}_{\mathrm{ps}}\boldsymbol{I}_{\mathrm{s}} \\ \boldsymbol{Y}_{\mathrm{C2}}\boldsymbol{U}_{\mathrm{s}} + \boldsymbol{B}\boldsymbol{I}_{\mathrm{s}} = \boldsymbol{I}_{\mathrm{sin}} \\ \boldsymbol{A}\boldsymbol{U}_{\mathrm{s}} = \boldsymbol{Z}_{\mathrm{s}}\boldsymbol{I}_{\mathrm{s}} + s\boldsymbol{M}_{s}\boldsymbol{I}_{s} + s\boldsymbol{M}_{\mathrm{ps}}\boldsymbol{I}_{\mathrm{p}} \end{cases} \tag{27}$$

where

$$\boldsymbol{A} = \begin{bmatrix} 1 & 0 & \cdots & 0 & 0 \\ -1 & 1 & \cdots & 0 & 0 \\ 0 & -1 & 1 & 0 & 0 \\ \vdots & \vdots & \cdots & \ddots & \vdots \\ 0 & 0 & \cdots & -1 & 1 \end{bmatrix},\ \boldsymbol{B} = \begin{bmatrix} 1 & -1 & 0 & \cdots & 0 \\ 0 & 1 & -1 & \cdots & 0 \\ 0 & 0 & \ddots & \cdots & \vdots \\ \vdots & \vdots & \cdots & 1 & -1 \\ 0 & 0 & \cdots & 0 & 1 \end{bmatrix} \tag{28}$$

$$\boldsymbol{Y}_{\mathrm{C1}} = \begin{bmatrix} \sum_{k=1,k\neq 2}^{n} Y_{\mathrm{Cp2},k} & \frac{-\mathrm{j}\omega C_{\mathrm{p2},3}}{1+\mathrm{j}\omega C_{1,2}R_{1,2}} & \cdots & \frac{-\mathrm{j}\omega C_{\mathrm{p2},n}}{1+\mathrm{j}\omega C_{2,n}R_{2,n}} \\ \frac{-\mathrm{j}\omega C_{\mathrm{p3},2}}{1+\mathrm{j}\omega C_{\mathrm{p3},2}R_{\mathrm{p3},2}} & \sum_{k=1,k\neq 3}^{n} Y_{\mathrm{Cp3},k} & \cdots & \frac{-\mathrm{j}\omega C_{\mathrm{p3},n}}{1+\mathrm{j}\omega C_{\mathrm{p3},n}R_{\mathrm{p3},n}} \\ \vdots & \vdots & \ddots & \vdots \\ \frac{-\mathrm{j}\omega C_{\mathrm{pn},2}}{1+\mathrm{j}\omega C_{\mathrm{pn},2}R_{\mathrm{pn},2}} & \frac{-\mathrm{j}\omega C_{\mathrm{pn},3}}{1+\mathrm{j}\omega C_{\mathrm{pn},3}R_{\mathrm{pn},3}} & \cdots & \sum_{k=1}^{n-1} Y_{\mathrm{Cpn},k} \end{bmatrix} \tag{29}$$

$$\boldsymbol{Y}_{\mathrm{C2}} = \begin{bmatrix} \sum_{k=1,k\neq 2}^{n} Y_{\mathrm{Cs2},k} & \frac{-\mathrm{j}\omega C_{\mathrm{s2},3}}{1+\mathrm{j}\omega C_{1,2}R_{1,2}} & \cdots & \frac{-\mathrm{j}\omega C_{\mathrm{s2},n}}{1+\mathrm{j}\omega C_{2,n}R_{2,n}} \\ \frac{-\mathrm{j}\omega C_{\mathrm{s3},2}}{1+\mathrm{j}\omega C_{\mathrm{s3},2}R_{\mathrm{s3},2}} & \sum_{k=1,k\neq 3}^{n} Y_{\mathrm{Cs3},k} & \cdots & \frac{-\mathrm{j}\omega C_{\mathrm{s3},n}}{1+\mathrm{j}\omega C_{\mathrm{s3},n}R_{\mathrm{s3},n}} \\ \vdots & \vdots & \ddots & \vdots \\ \frac{-\mathrm{j}\omega C_{sn,2}}{1+\mathrm{j}\omega C_{sn,2}R_{sn,2}} & \frac{-\mathrm{j}\omega C_{sn,3}}{1+\mathrm{j}\omega C_{sn,3}R_{sn,3}} & \cdots & \sum_{k=1}^{n-1} Y_{\mathrm{Csn},k} \end{bmatrix} \tag{30}$$

$$\boldsymbol{Z}_{\mathrm{p}} = \begin{bmatrix} sL_{\mathrm{p1}}+R_{L\mathrm{p1}} & 0 & \cdots & 0 \\ 0 & sL_{\mathrm{p2}}+R_{L\mathrm{p2}} & \cdots & 0 \\ \vdots & \vdots & \ddots & \vdots \\ 0 & 0 & \cdots & sL_{\mathrm{pn}}+R_{L\mathrm{pn}} \end{bmatrix} \tag{31}$$

$$\boldsymbol{Z}_{\mathrm{s}} = \begin{bmatrix} sL_{\mathrm{s1}}+R_{L\mathrm{p1}} & 0 & \cdots & 0 \\ 0 & sL_{\mathrm{s2}}+R_{L\mathrm{p2}} & \cdots & 0 \\ \vdots & \vdots & \ddots & \vdots \\ 0 & 0 & \cdots & sL_{sn}+R_{L\mathrm{pn}} \end{bmatrix} \tag{32}$$

$$\boldsymbol{U}_{\mathrm{p}}=\begin{bmatrix}U_{\mathrm{p1}}\\U_{\mathrm{p2}}\\\vdots\\U_{\mathrm{p}n}\end{bmatrix},\ \boldsymbol{U}_{\mathrm{s}}=\begin{bmatrix}U_{\mathrm{s1}}\\U_{\mathrm{s2}}\\\vdots\\U_{\mathrm{s}n}\end{bmatrix} \tag{33}$$

$$\boldsymbol{I}_{\mathrm{p}}=\begin{bmatrix}I_{\mathrm{p1}}\\I_{\mathrm{p2}}\\\vdots\\I_{\mathrm{p}n}\end{bmatrix},\ \boldsymbol{I}_{\mathrm{s}}=\begin{bmatrix}I_{\mathrm{s1}}\\I_{\mathrm{s2}}\\\vdots\\I_{\mathrm{s}n}\end{bmatrix},\ \boldsymbol{I}_{\mathrm{pin}}=\begin{bmatrix}I_{\mathrm{pin}}\\0\\\vdots\\0\end{bmatrix},\ \boldsymbol{I}_{\mathrm{sin}}=\begin{bmatrix}I_{\mathrm{sin}}\\0\\\vdots\\0\end{bmatrix} \tag{34}$$

$$M_{\mathrm{p}}=\begin{bmatrix}0&M_{\mathrm{p}1,2}&\cdots&M_{\mathrm{p}1,n}\\M_{\mathrm{p}2,1}&0&\cdots&M_{\mathrm{p}2,n}\\\vdots&\vdots&\ddots&\vdots\\M_{\mathrm{p}n,1}&M_{\mathrm{p}n,2}&\cdots&0\end{bmatrix},$$

$$M_{\mathrm{s}}=\begin{bmatrix}0&M_{\mathrm{s}1,2}&\cdots&M_{\mathrm{s}1,n}\\M_{\mathrm{s}2,1}&0&\cdots&M_{\mathrm{s}2,n}\\\vdots&\vdots&\ddots&\vdots\\M_{\mathrm{s}n,1}&M_{\mathrm{s}n,2}&\cdots&0\end{bmatrix} \tag{35}$$

$$M_{\mathrm{ps}}=\begin{bmatrix}M_{\mathrm{p1s1}}&M_{\mathrm{p1s2}}&\cdots&M_{\mathrm{p1sn}}\\M_{\mathrm{p2s1}}&M_{\mathrm{p2s2}}&\cdots&M_{\mathrm{p2sn}}\\\vdots&\vdots&\ddots&\vdots\\M_{\mathrm{pns1}}&M_{\mathrm{pns2}}&\cdots&M_{\mathrm{pnsn}}\end{bmatrix}. \tag{36}$$

From (27)–(36), the impedance parameter (Z parameter) matrix of network N_2 can be expressed as

$$\boldsymbol{Z}_{\mathrm{N2}}=\begin{bmatrix}Z_{11}&Z_{12}\\Z_{21}&Z_{22}\end{bmatrix} \tag{37}$$

where Z_{11}, Z_{12}, $Z_{21,}$ and Z_{22} can be calculated as (38)shown at the bottom of this page.

The ABCD parameters of N_2 can be converted from Z petameters, then $\boldsymbol{A_{N2}}$ can be expressed as

$$\boldsymbol{A}_{\mathrm{N2}}=\begin{bmatrix}A''&B''\\C''&D''\end{bmatrix}=\begin{bmatrix}\frac{Z_{11}}{Z_{21}}&\frac{Z_{11}Z_{22}-Z_{12}Z_{21}}{Z_{21}}\\\frac{1}{Z_{21}}&\frac{Z_{22}}{Z_{21}}\end{bmatrix}. \tag{39}$$

The ABCD parameter matrix of the two-port network shown in Fig. 13 can be calculated by (25)–(38) as

$$\boldsymbol{A}_{\mathrm{N}}=\boldsymbol{A}_{\mathrm{N1}}\boldsymbol{A}_{\mathrm{N2}}\boldsymbol{A}_{\mathrm{N3}} \tag{40}$$

U_{TXp}, I_{TXp}, $U_{\mathrm{RXp,}}$ and I_{RXp} can be obtained by (40) as

$$\begin{bmatrix}U_{\mathrm{TXp}}\\I_{\mathrm{TXp}}\end{bmatrix}=\boldsymbol{A}_{\mathrm{N}}\begin{bmatrix}U_{\mathrm{RXs}}\\-I_{\mathrm{RXs}}\end{bmatrix}=\boldsymbol{A}_{\mathrm{N1}}\boldsymbol{A}_{\mathrm{N2}}\boldsymbol{A}_{\mathrm{N3}}\begin{bmatrix}U_{\mathrm{RXs}}\\-I_{\mathrm{RXs}}\end{bmatrix}. \tag{41}$$

From (40), the voltage gain of the data channel can be expressed as

$$G_{\mathrm{d}}=\frac{U_{\mathrm{RXs}}}{U_{\mathrm{TXp}}}=\frac{1}{[\boldsymbol{A}_{\mathrm{N}}]_{11}}=\frac{1}{[\boldsymbol{A}_{\mathrm{N1}}\boldsymbol{A}_{\mathrm{N2}}\boldsymbol{A}_{\mathrm{N3}}]_{11}}. \tag{42}$$

According to the symmetry of system, the forward gain G_{dp} and reverse gain G_{ds} of the data channel can be expressed as

$$\begin{cases}G_{\mathrm{dp}}=G_{\mathrm{d}}(\omega_{\mathrm{dp}})\\G_{\mathrm{ds}}=G_{\mathrm{d}}(\omega_{\mathrm{ds}})\end{cases} \tag{43}$$

where ω_{dp} (ω_{ds}) is the frequency of forward (backward) data channel.

The relationship between G_{dp} (G_{ds}) and frequency under the different C_{dp1} (C_{ds1}) and C_{dp2} (C_{ds2}) is shown in Fig. 14(a). There are two extreme points for the voltage gain of the communication channel. For different C_{dp1} (C_{ds1}) and C_{dp2} (C_{ds2}), the values of these two extreme points will be different. Fig. 14(b) shows the relationship of two extreme values, G_{df1} and $G_{\mathrm{df2,}}$ with different C_{dp1} (C_{ds1}) and C_{dp2} (C_{ds2}). The area enclosed by the dotted line has a gain greater than 0.45. Therefore, C_{dp1} (C_{ds1}) and C_{dp2} (C_{ds2}) are designed as 0.22 nF (0.22 nF) and 1 nF (1 nF) in the proposed system. When the tolerance of the capacitor is 5% or 10%, the voltage gain of the data channel can still reach more than 0.45, which can meet the system requirements.

For the data channel, voltage gain at two resonant frequencies varies with the radial misalignment and axial misalignment is shown in Fig. 15. Fig. 15 shows that as the misalignment increases, the voltage gain of data channel gradually decreases. With the fluctuation of water flow, the voltage gain of the data channel will also fluctuate. Within a certain range, the gain of the

$$\begin{cases}Z_{11}=\left.\frac{U_{\mathrm{inp}}}{I_{\mathrm{inp}}}\right|_{I_{\mathrm{ins}}=0}=\left\{\boldsymbol{Y}_{\mathrm{C1}}+\boldsymbol{B}\left[\boldsymbol{Z}_{\mathrm{p}}+s\boldsymbol{M}_{\mathrm{p}}-s^2\boldsymbol{M}_{\mathrm{ps}}^2\boldsymbol{B}^{-1}\boldsymbol{Y}_{\mathrm{C2}}\left(\boldsymbol{A}+\boldsymbol{Z}_{\mathrm{s}}\boldsymbol{B}^{-1}\boldsymbol{Y}_{\mathrm{C2}}+s\boldsymbol{M}_{\mathrm{s}}\boldsymbol{B}^{-1}\boldsymbol{Y}_{\mathrm{C2}}\right)^{-1}\right]^{-1}\right\}_{11}^{-1}\\Z_{21}=\left.\frac{U_{\mathrm{ins}}}{I_{\mathrm{inp}}}\right|_{I_{\mathrm{ins}}=0}=\Big[\boldsymbol{Y}_{\mathrm{C1}}\boldsymbol{A}^{-1}\left(\boldsymbol{Z}_{\mathrm{p}}+s\boldsymbol{M}_{\mathrm{p}}\right)\boldsymbol{M}_{\mathrm{ps}}^{-1}\left(s^{-1}\boldsymbol{A}+s^{-1}\boldsymbol{Z}_{\mathrm{s}}\boldsymbol{B}^{-1}\boldsymbol{Y}_{\mathrm{C2}}+\boldsymbol{M}_{\mathrm{s}}\boldsymbol{B}^{-1}\boldsymbol{Y}_{\mathrm{C2}}-\boldsymbol{M}_{\mathrm{ps}}\boldsymbol{B}^{-1}\boldsymbol{Y}_{\mathrm{C2}}\right)\\+\boldsymbol{B}\boldsymbol{M}_{\mathrm{ps}}^{-1}\left(s^{-1}\boldsymbol{A}+s^{-1}\boldsymbol{Z}_{\mathrm{s}}\boldsymbol{B}^{-1}\boldsymbol{Y}_{\mathrm{C2}}+\boldsymbol{M}_{\mathrm{s}}\boldsymbol{B}^{-1}\boldsymbol{Y}_{\mathrm{C2}}\right)\Big]_{11}^{-1}\\Z_{12}=\left.\frac{U_{\mathrm{inp}}}{I_{\mathrm{ins}}}\right|_{I_{\mathrm{inp}}=0}=\Big[\boldsymbol{Y}_{\mathrm{C2}}\boldsymbol{A}^{-1}\left(\boldsymbol{Z}_{\mathrm{s}}+s\boldsymbol{M}_{\mathrm{s}}\right)\boldsymbol{M}_{\mathrm{ps}}^{-1}\left(s^{-1}\boldsymbol{A}+s^{-1}\boldsymbol{Z}_{\mathrm{p}}\boldsymbol{B}^{-1}\boldsymbol{Y}_{\mathrm{C1}}+\boldsymbol{M}_{\mathrm{p}}\boldsymbol{B}^{-1}\boldsymbol{Y}_{\mathrm{C1}}-\boldsymbol{M}_{\mathrm{ps}}\boldsymbol{B}^{-1}\boldsymbol{Y}_{\mathrm{C1}}\right)\\+\boldsymbol{B}\boldsymbol{M}_{\mathrm{ps}}^{-1}\left(s^{-1}\boldsymbol{A}+s^{-1}\boldsymbol{Z}_{\mathrm{p}}\boldsymbol{B}^{-1}\boldsymbol{Y}_{\mathrm{C1}}+\boldsymbol{M}_{\mathrm{p}}\boldsymbol{B}^{-1}\boldsymbol{Y}_{\mathrm{C1}}\right)\Big]_{11}^{-1}\\Z_{22}=\left.\frac{U_{\mathrm{ins}}}{I_{\mathrm{ins}}}\right|_{I_{\mathrm{inp}}=0}=\left\{\boldsymbol{Y}_{\mathrm{C2}}+\boldsymbol{B}\left[\boldsymbol{Z}_{\mathrm{s}}+s\boldsymbol{M}_{\mathrm{s}}-s^2\boldsymbol{M}_{\mathrm{ps}}^2\boldsymbol{B}^{-1}\boldsymbol{Y}_{\mathrm{C1}}\left(\boldsymbol{A}+\boldsymbol{Z}_{\mathrm{p}}\boldsymbol{B}^{-1}\boldsymbol{Y}_{\mathrm{C1}}+s\boldsymbol{M}_{\mathrm{p}}\boldsymbol{B}^{-1}\boldsymbol{Y}_{\mathrm{C1}}\right)^{-1}\right]^{-1}\right\}_{11}^{-1}\end{cases} \tag{38}$$

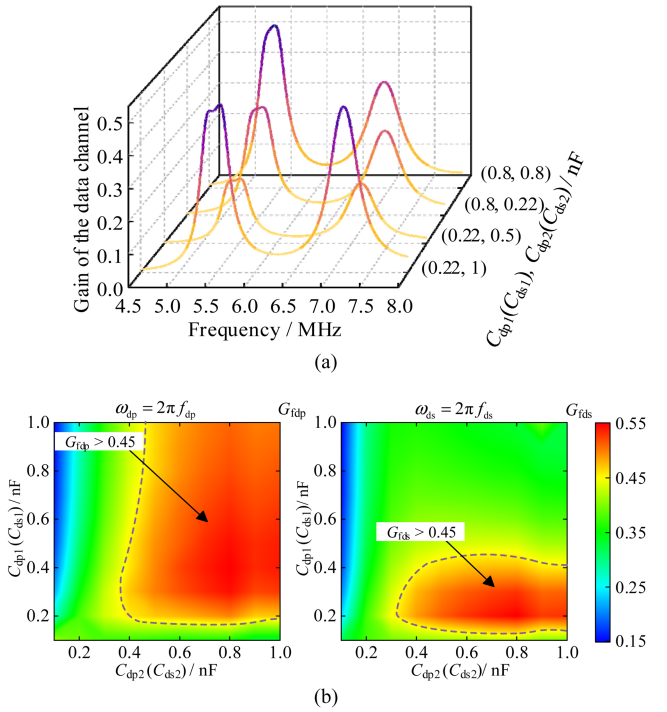

Fig. 14. Relationship between G_d, frequency and C_{dp1} (C_{ds1}), C_{dp2} (C_{ds2}). (a) Gain of data channel versus frequency and $C_{dp1}(C_{ds1})$, $C_{dp2}(C_{ds2})$. (b) G_{fdp} (G_{fds}) versus C_{dp1} (C_{ds1}), C_{dp2} (C_{ds2}) at f_p (f_s).

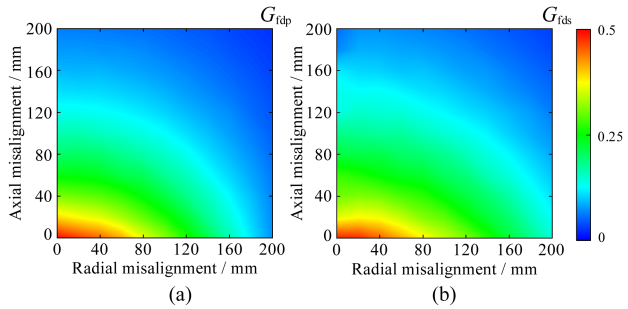

Fig. 15. Voltage gain at two resonant frequencies of data channel varies with the radial misalignment and axial misalignment. (a) Voltage gain of data channel at the first frequency. (b) Voltage gain of data channel at the second frequency.

data channel can reach more than 0.2. The operational amplifier used in this article is LM7171, and its gain bandwidth product can reach 200 MHz, so the fluctuation of water will not affect the data transmission after the fixed device is installed.

The center frequencies of the two frequency bands in the data channel are 5.4 and 7.3 MHz, respectively. Therefore, in forward transmission, 5.4 MHz represents 1 and 5.6 MHz represents 0. In reverse transmission, 7.3 MHz represents 1 and 7.5 MHz represents 0. From the above-mentioned analysis, two frequency bands can achieve independent transmission, so this article achieves full-duplex data transmission.

According to the Shannon–Hartley theorem, the theoretical maximum data rate is related to data transfer power, noise power, and channel bandwidth [10]. The modulation method used in this article is FSK. Its principle is to distinguish 0 and 1 according

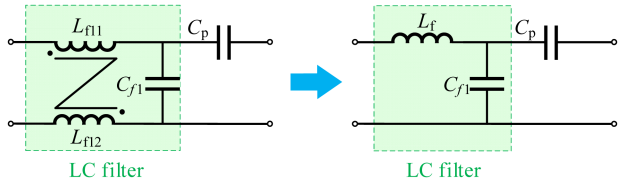

Fig. 16. Equivalent circuit of *LLCC* compensation for differential mode interference.

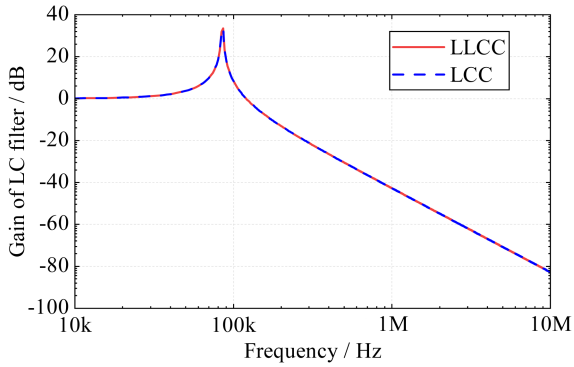

Fig. 17. Gain of LC filter.

to the different output frequencies. Therefore, its theoretical maximum data rate is 2/*f*, where *f* is the center frequency of the carrier. To reduce the bit error rate, this article detects more than 10 cycles to determine the output.

V. Crosstalk Analysis

The interference of the data channel comes from rapid switching, power signal, and ipsilateral data signal. The CM interference is mainly caused by the fast switching of semiconductor devices and the parasitic capacitances of devices to the reference ground in the proposed USWPDT system.

A. Suppression of Differential Mode Interference

Taking the primary side as an example, the two inductors L_{f11} and L_{f22} in *LLCC* compensation can be equivalent to one inductor L_{f1} for differential mode interference from (2)–(5). Therefore, for differential mode interference, *LLCC* compensation can be equivalent to *LCC* compensation topology, as shown in Fig. 16. In the *LCC* compensation topology, the LC forms a second-order lowpass filter, and its amplitude-frequency characteristics are shown in Fig. 17. So *LLCC* and *LCC* compensation topology have a significant suppression effect on high-frequency differential-mode interference. And their suppression principle and effect on differential mode interference are the same in theory.

B. Suppression of Common Mode Interference

The principle and difference of *LLCC* compensation and T-type compensation topologies for CM interference suppression are analyzed. The point B of the T type topology in Fig. 18(b) is the inverter output, which is directly connected to the coil. The

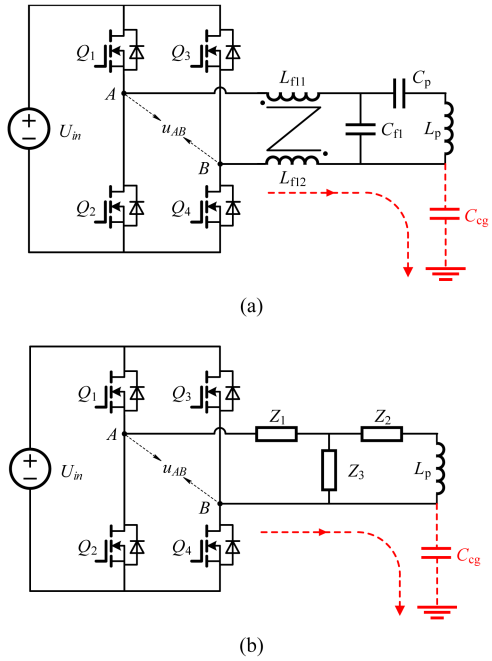

Fig. 18. Common mode current of *LLCC* compensation and T-type compensation. (a) *LLCC* compensation topology. (b) T-type compensation topology.

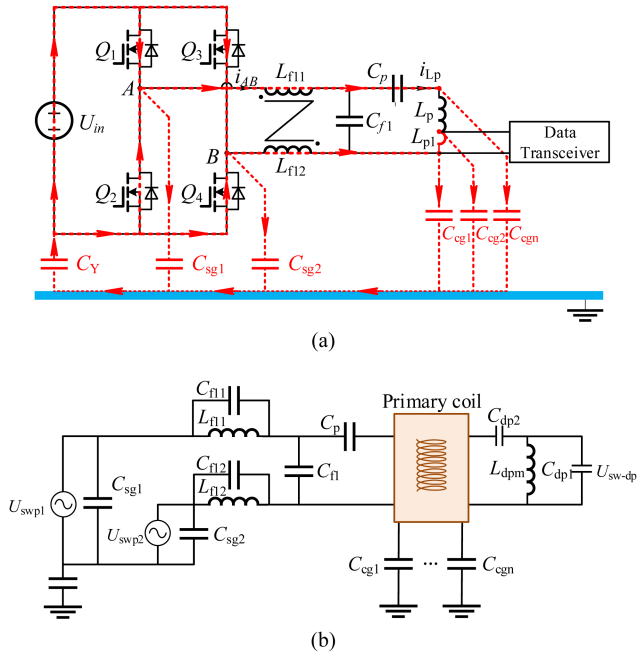

Fig. 19. High-frequency coupling paths of CM EMI on the primary side. (a) High-frequency coupling paths. (b) Equivalent circuit of CM EMI.

common mode current flows from the inverter directly to the ground through the stray capacitance of the coil to ground, and the path is shown in Fig. 18(b). The point B in the *LLCC* topology in Fig. 18(a) is the inverter output, which is connected to the compensation inductor. The common mode current flows to the ground through compensating inductor and parasitic capacitors of coil, as shown in Fig. 18(a). The compensating inductor and stray capacitor form a second-order lowpass filter, which has a significant suppression effect on common mode interference at high frequencies.

The more specific high-frequency coupling paths of CM EMI on the primary side are shown in Fig. 19(a). The red arrow indicates the path of the system CM current. $C_{\rm Y}$ represents the Y-capacitor on the dc side. The parasitic capacitances from the drain of the low-side MOSFETs to the reference ground are $C_{\rm sg1}$ and $C_{\rm sg2}$. $C_{\rm cg1}$, $C_{\rm cg2}$, and $C_{\rm cg3}$ represent the distributed capacitances of the coil to the reference ground. The dc power supply can be regarded as a short circuit. The CM current flows into the reference ground through $C_{\rm sg1}$, $C_{\rm sg2}$, $C_{\rm cg1}$, $C_{\rm cg2}$, and $C_{\rm cg3}$, then returns through the $C_{\rm Y}$ to form a current loop. To analyze the influence of the power channel on the data channel, the circuit in Fig. 19(a) can be simplified to Fig. 19(b) [38]. $C_{\rm f11}$ ($C_{\rm f12}$) is the parasitic capacitance of $L_{\rm f11}$ ($L_{\rm f12}$). $U_{\rm sw\text{-}dp}$ is the voltage of $C_{\rm dp1}$. The phase difference between $U_{\rm sw1}$ and $U_{\rm sw2}$ is 180°.

When the amplitude of $U_{\rm sw1}$ and $U_{\rm sw2}$ is 1 V. The relationship between different $L_{\rm f11}$, $L_{\rm f12}$, and the voltage $U_{\rm sw\text{-}dp}$ generated by CM interference is shown in Fig. 20. Since the circuit parameters of the primary and secondary sides are the same, the voltages $U_{\rm sw\text{-}dp}$ and $U_{\rm sw\text{-}ds}$ generated

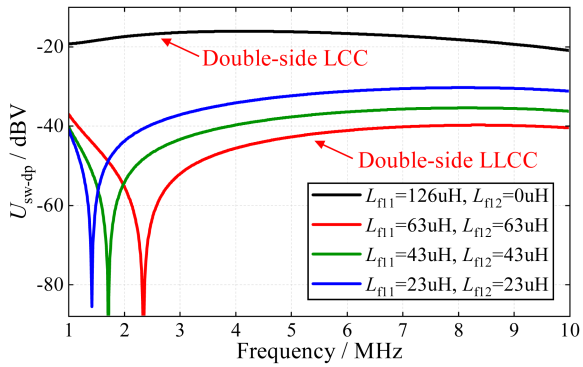

Fig. 20. Attenuation of CM EMI versus frequency at different $L_{\rm f11}$ and $L_{\rm f22}$.

by the CM interference on the primary and secondary sides are −40 dBV, while the interference voltage generated by the traditional *LCC* compensation is −17 dB at 7.3 MHz. Therefore, the double-side *LLCC* proposed in this article can suppress common mode interference by more than 40 dB, while *LCC* is less than 20 dB.

The coupling coils in Fig. 3(a) can be simplified to Fig. 21(a). The theoretical analysis in Section III shows that the data channel has little influence on the power channel. Therefore, the voltage on $L_{\rm p1}$ ($L_{\rm s1}$) can be regarded as an independent voltage source for the input port of the data transceiver, as shown in Fig. 21(b). The $U_{\rm Lp1}$ and $U_{\rm Ls1}$ can be expressed as

$$\begin{cases} U_{\rm Lp1} = j\omega_{\rm p}(L_{\rm p1}+M_{\rm p1p2})I_{\rm Lp} - j\omega_{\rm p}(M_{\rm p2s1}+M_{\rm p2s2})I_{\rm Ls} \\ U_{\rm Ls1} = j\omega_{\rm p}(L_{\rm s1}+M_{\rm s1s2})I_{\rm Ls} - j\omega_{\rm p}(M_{\rm p1s2}+M_{\rm p2s2})I_{\rm Lp} \end{cases} . \tag{44}$$

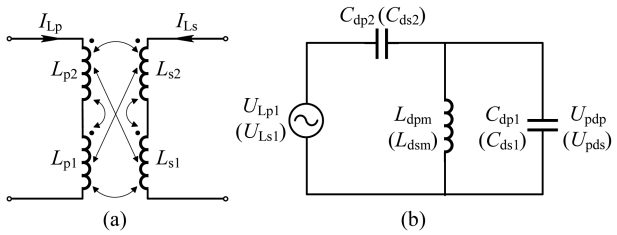

Fig. 21. Equivalent circuit of coupling coils and transceiver. (a) Equivalent circuit of the coupling coils. (b) Influence of the last turn on the transceiver.

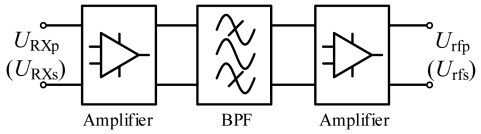

Fig. 22. Bandpass filter.

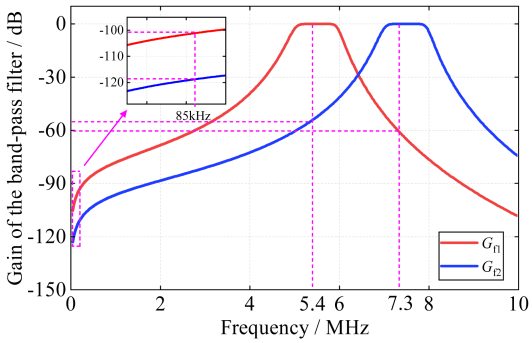

Fig. 23. Gain of bandpass filter versus frequency.

The interference voltage U_{pdp} (U_{pds}) generated by the primary (secondary) coil to the primary (secondary) data transceiver can be calculated as

$$\begin{cases} U_{\mathrm{pdp}} = \dfrac{U_{\mathrm{Lp1}} Z_{\mathrm{dp}}}{Z_{\mathrm{dp}} + 1/j\omega_{\mathrm{p}} C_{\mathrm{dp2}}} \\ U_{\mathrm{pds}} = \dfrac{U_{\mathrm{Ls1}} Z_{\mathrm{ds}}}{Z_{\mathrm{ds}} + 1/j\omega_{\mathrm{p}} C_{\mathrm{ds2}}} \end{cases} \tag{45}$$

where

$$\begin{cases} Z_{\mathrm{dp}} = \dfrac{j\omega_{\mathrm{p}} L_{\mathrm{dpm}} (1/j\omega_{\mathrm{p}} C_{\mathrm{dp1}})}{j\omega_{\mathrm{p}} L_{\mathrm{dpm}} + 1/j\omega_{\mathrm{p}} C_{\mathrm{dp1}}} = \dfrac{j\omega_{\mathrm{p}} L_{\mathrm{dpm}}}{1 - \omega_{\mathrm{p}}^2 L_{\mathrm{dpm}} C_{\mathrm{dp1}}} \\ Z_{\mathrm{ds}} = \dfrac{j\omega_{\mathrm{p}} L_{\mathrm{dsm}} (1/j\omega_{\mathrm{p}} C_{\mathrm{ds1}})}{j\omega_{\mathrm{p}} L_{dsm} + 1/j\omega_{\mathrm{p}} C_{\mathrm{ds1}}} = \dfrac{j\omega_{\mathrm{p}} L_{\mathrm{dsm}}}{1 - \omega_{\mathrm{p}}^2 L_{\mathrm{dsm}} C_{\mathrm{ds1}}} \end{cases} . \tag{46}$$

When the proposed USWPDT system works at 500 W, the values of U_{pdp} and U_{pds} are hundreds of millivolts. Therefore, the interference of the power signal and ipsilateral data signal can be filtered out by a bandpass filter, as shown in Fig. 22.

U_{rfp} (U_{rfs}) is the output voltage of the filter. The amplitude-frequency characteristic curves of the bandpass filter in the primary and secondary are shown in Fig. 23. The power signal of 85 kHz is attenuated by more than 100 dB. The ipsilateral data signal is attenuated by more than 50 dB.

After bandpass filtering, the power signal and ipsilateral data signal can be ignored. Therefore, the interference mainly comes from the switching moment of MOSFET and diodes. The forward

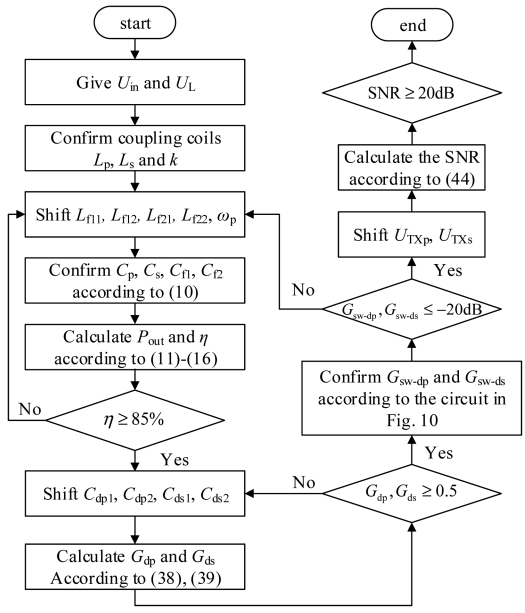

Fig. 24. Design flowchart of power and data channel.

and backward SNRs of the proposed SWPDT system is calculated as

$$\begin{cases} \mathrm{SNR_p} = \dfrac{U_{\mathrm{TXp}} G_{\mathrm{dp}}(\omega_{\mathrm{dp}})}{U_{\mathrm{sw-dp}}} \\ \mathrm{SNR_s} = \dfrac{U_{\mathrm{TXs}} G_{\mathrm{ds}}(\omega_{\mathrm{ds}})}{U_{\mathrm{sw-ds}}} \end{cases} . \tag{47}$$

VI. Design Method for Power and Data Transfer

To satisfy the requirements of high-efficiency power transfer and high-speed data transfer, the SWPDT system needs to achieve the objectives as shown in (48). The PTE should be above 85%. The switching noise attenuation should be above 20 dB. The voltage gain of the forward and backward data channel should be above 0.45. The SNR should be above 20 dB

$$\begin{cases} \eta \geq 85\% \\ G_{\mathrm{sw-dp}}, G_{\mathrm{sw-ds}} \leq -20\,\mathrm{dB} \\ G_{\mathrm{dp}}, G_{\mathrm{ds}} \geq 0.45 \\ \mathrm{SNR} \geq 20\,\mathrm{dB} \end{cases} . \tag{48}$$

The flow chart of system parameter design and optimization is shown in Fig. 24. For the USWPDT system, the transfer distance is usually fixed due to the mechanical fixing of the charging dock. The actual system determines the input voltage, load, and coupling coils. The frequency and compensation parameters can be selected to satisfy the requirement of output power and PTE according to (11)–(16). The capacitors (C_{dp1}, C_{dp2}, C_{ds1}, and C_{ds2}) in data transceivers can be designed to make the voltage gain (G_{dp}, G_{ds}) of the data channel more than 0.45 according to (42) and (43). Then the attenuation ($G_{\mathrm{sw\text{-}dp}}$, $G_{\mathrm{sw\text{-}ds}}$) of switching noise is calculated using the current parameters of the power channel and data channel. To attenuate the switching noise by more than 20 dB, the compensation parameters of the power channel and capacitors in data transceivers need to be adjusted

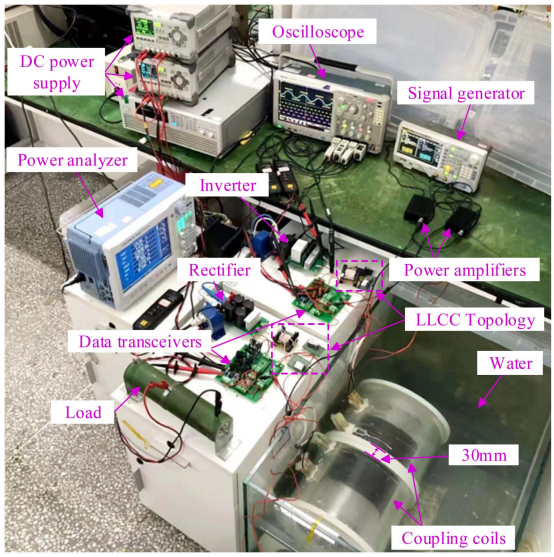

Fig. 25. Experimental platform.

TABLE II
MAIN PARAMETERS UTILIZED IN EXPERIMENT

Symbol	Value	Symbol	Value
U_{in}	126V	C_{f1}, C_{f2}	27.8nF
R_L	287Ω	C_p, C_s	11.9nF
f_p	85kHz	L_p, L_s	418uH
L_{f11}, L_{f12}, L_{f21}, L_{f22}	32.5uH	M	123uH
k_{fp}, k_{fs}	0.94	M_{p1p2}, M_{s1s2}	7.91uH, 7.95uH
C_{dp1}, C_{ds1}	220pF	L_{p1}, L_{s1}	1uH, 1.1uH
C_{dp2}, C_{ds2}	1nF	M_{p1s1}	26nH
L_{dpm}, L_{dsm}	7.3uH	M_{p2s2}	120uH
f_{dp}	5.4MHz	M_{p1s2}, M_{p2s1}	1.6uH, 1.5uH
f_{ds}	7.3MHz	R_p, R_s	590mΩ, 605mΩ

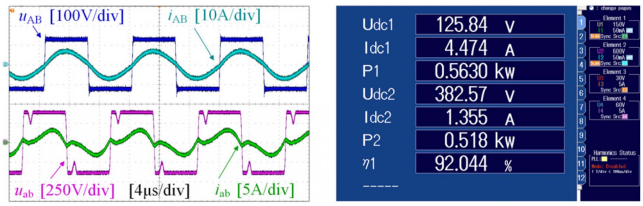

(a) (b)

Fig. 26. Voltage, current, power, and efficiency when $U_{in} = 126$ V and $R = 287\ \Omega$. (a) Waveforms of power transfer. (b) Power and efficiency on the dc side.

again. Finally, the voltage of data carriers U_{TXp} and U_{TXs} are adjusted to achieve the requirement of SNR.

VII. EXPERIMENTAL VERIFICATION

A 518-W prototype was built following the design flowchart in Section VI, as shown in Fig. 25. The parameters of the proposed SWPDT system are listed in Table II. The size of the coupling coils is $\Phi 30 \times 20$ cm, and the transmission distance is 30 mm. The scheme of data modulation is FSK.

According to the design procedure in Fig. 24, the power transfer frequency is 85 kHz. The waveforms of power transfer are shown in Fig. 26. Fig. 26(a) shows the waveforms of u_{AB}, i_{AB}, u_{ab}, and i_{ab}. Fig. 26(b) shows output power is 518 W, and the PTE of the system is 92%. The MOSFETs of the inverter achieve ZVS.

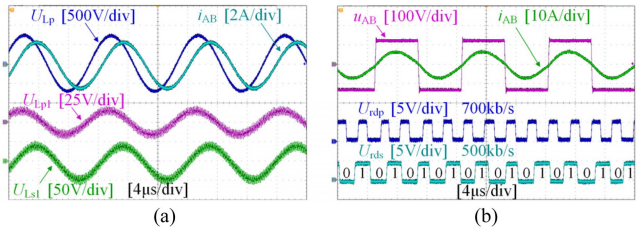

(a) (b)

Fig. 27. Waveforms of power and data channel. (a) Waveforms of U_{Lp}, i_{AB}, U_{Lp1}, U_{Ls1}. (b) u_{AB}, i_{AB}, U_{rdp}, U_{rds}.

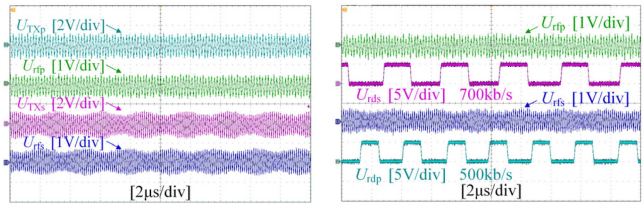

(a) (b)

Fig. 28. Waveforms of data transfer. (a) Waveforms of U_{TXp}, U_{rfp}, U_{TXs}, U_{rfs}. (b) Waveforms of U_{rfp}, U_{rds}, U_{rfs} and U_{rdp}.

Fig. 27 shows the waveforms of U_{Lp}, i_{AB}, U_{Lp1}, and U_{Ls1}. The data carriers are rarely observed in the waveforms of U_{Lp} and i_{AB}. U_{Lp1} and U_{Ls1} superimpose the high-frequency carrier of the data channel at the frequency of 85 kHz. The amplitudes of U_{Lp1} and U_{Ls1} are 20 V and 50 V, respectively. It shows that the data channel has little influence on the power channel. The power channel applies a relatively low voltage to the channel, which reduces the voltage stress of the data channel. The waveforms of sending and receiving data when the system is in full-duplex communication are shown in Fig. 27(b). The forward and backward data rates are 500 and 700 kb/s, respectively.

Fig. 28(a) shows the waveforms of modulated signals U_{TXp}, U_{TXs}, and received signals U_{rfp}, U_{rfs}. The gains of forward and backward data channels are both 0.5, consistent with the analysis in Section IV and the computational results in Fig. 14. The data channel is demodulated by FSK, as shown in Fig. 28(b).

The spectrum of the switching instant is rich. Taking the primary side as an example, the continuous wavelet transform of u_{AB} is performed to obtain the spectrum distribution at each moment, as shown in Fig. 29. The area surrounded by the dotted line is the cone of influence, which does not affect the analysis of switching noise. The area covered by magenta dots is the switching noise in the communication frequency band.

Fig. 30 shows the switching moment of the inverter and rectifier and the influence on the data channel. At the switching instant, the amplitude of the data channel only changes by up to 0.1 V. Therefore, the SNR of the proposed USWPT system is 20 dB. In order to observe the interference on the primary receiving side more intuitively when using *LLCC* compensation, Fig. 31 shows the waveforms of the primary data receiving side at the switching moment when no data is being transferred. At the moment of switching, the interference on the data receiving side is particularly small. Fig. 32 shows the waveform of the data

TABLE III
COMPARISON BETWEEN DIFFERENT WORKS

Reference	This paper	[24]	[25]	[28]	[26]	[21]
P_{out}	518W	500W	400W	300W	600W	290W
PTE	92%	84%	86%	90%	85%	95%
Communication mode	Full-duplex	Full-duplex	Full-duplex	Full-duplex	Full-duplex	Half-duplex
Modulation	FSK	ASK	ASK	FSK	ASK	FSK
Forward data rate	500kb/s	200kb/s	100kb/s	500kb/s	80kb/s	150kb/s
Backward data rate	700kb/s	600kb/s	200kb/s	500kb/s	80kb/s	150kb/s
Withstand voltage of transceivers	>20V/>50V	>700V/>500V	>500V/>500V	>150V/>200V	>150V/>100V	>96V/>115V
SNR	20dB	32dB	27dB	20dB	8.6dB	47dB
Number of components connected with power channel	4	8	16	4	12	2
CM interference attenuation	-40dB	Not analysis	Not analysis	Not analysis	Not analysis	Not analysis

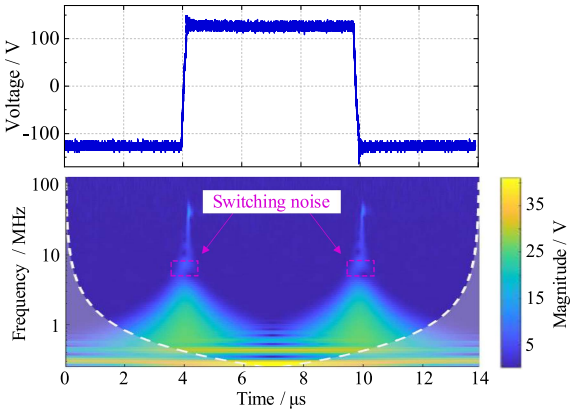

Fig. 29. Frequency spectrum of inverter output.

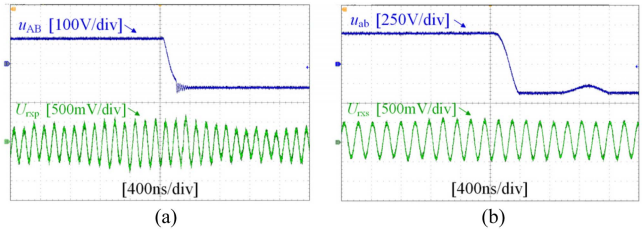

Fig. 30. Interference of power channel to data channel under the proposed double-side *LLCC* compensation. (a) Primary side. (b) Secondary side.

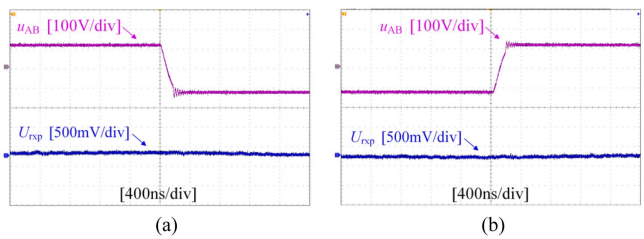

Fig. 31. Interference of power channel to data channel under double-side *LLCC* compensation when no data is being transferred. (a) At the moment of the falling edge of u_{AB}. (b) At the moment of the rising edge of u_{AB}.

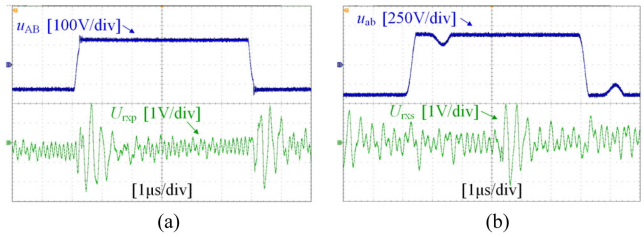

Fig. 32. Interference of power channel to data channel under double-side *LCC* compensation. (a) Primary side. (b) Secondary side.

channel at the instant of switching on the primary and secondary sides when using traditional double-side *LCC* compensation. The SNR is −10.9 dB. The double-side *LLCC* compensation proposed in this article suppresses CM interference and improves SNR significantly.

The comparison between some typical reported and proposed SWPDT systems are listed in Table III. The proposed USWPT system realizes 518 W output power with PTE of 92% and 500 kbps/700 kbps full-duplex communication mode. The withstand voltage of transceivers is reduced and the number of components connected with the power channel is only four, which can improve the reliability of the system. The proposed *LLCC* compensation can significantly suppress the CM interference to the data channel without increasing the size and loss of the system.

VIII. CONCLUSION

This article proposed a novel USWPDT system. The double-side *LLCC* compensation topology with the same size as double-side *LCC* topology and limited extra loss is proposed to suppress CM interference to the data channel generated from the power channel. The novel system structure reduces the voltage stress of the data channel and the number of components directly connected with the power channel. The design method of the power and data transfer channel is proposed. Finally, the prototype realizes the synchronous transfer of power and data with an output power of 518 W, efficiency of 92%, and 500 kbps/700 kbps full-duplex communication.

REFERENCES

[1] C. R. Teeneti, T. T. Truscott, D. N. Beal, and Z. Pantic, "Review of wireless charging systems for autonomous underwater vehicles," *IEEE J. Ocean. Eng.*, vol. 46, no. 1, pp. 68–87, Jan. 2021, doi: 10.1109/JOE.2019.2953015.

[2] A. M. Bradley, M. D. Feezor, H. Singh, and F. Y. Sorrell, "Power systems for autonomous underwater vehicles," *IEEE J. Ocean. Eng.*, vol. 26, no. 4, pp. 526–538, Oct. 2001, doi: 10.1109/48.972089.

[3] D. Wang, S. Cui, J. Zhang, Z. Bie, K. Song, and C. Zhu, "A novel arc-shaped lightweight magnetic coupler for AUV wireless power transfer," *IEEE Trans. Ind. Appl.*, vol. 58, no. 1, pp. 1315–1329, Jan./Feb. 2022, doi: 10.1109/TIA.2021.3109839.

[4] C. Cai, S. Wu, Z. Zhang, L. Jiang, and S. Yang, "Development of a fit-to-surface and lightweight magnetic coupler for autonomous underwater vehicle wireless charging systems," *IEEE Trans. Power Electron.*, vol. 36, no. 9, pp. 9927–9940, Sep. 2021, doi: 10.1109/TPEL.2021.3064411.

[5] T. Kan, R. Mai, P. P. Mercier, and C. C. Mi, "Design and analysis of a three-phase wireless charging system for lightweight autonomous underwater vehicles," *IEEE Trans. Power Electron.*, vol. 33, no. 8, pp. 6622–6632, Aug. 2018, doi: 10.1109/TPEL.2017.2757015.

[6] Z. Yan, B. Song, Y. Zhang, K. Zhang, Z. Mao, and Y. Hu, "A rotation-free wireless power transfer system with stable output power and efficiency for autonomous underwater vehicles," *IEEE Trans. Power Electron.*, vol. 34, no. 5, pp. 4005–4008, May 2019, doi: 10.1109/TPEL.2018.2871316.

[7] T. Orekan, P. Zhang, and C. Shih, "Analysis, design, and maximum power-efficiency tracking for undersea wireless power transfer," *IEEE J. Emerg. Sel. Topics Power Electron.*, vol. 6, no. 2, pp. 843–854, Jun. 2018, doi: 10.1109/JESTPE.2017.2735964.

[8] Y. Yang, Y. Xiao, and T. Li, "A survey of autonomous underwater vehicle formation: Performance, formation control, and communication capability," *IEEE Commun. Surv. Tut.*, vol. 23, no. 2, pp. 815–841, Apr.–Jun. 2021, doi: 10.1109/COMST.2021.3059998.

[9] R. Mai, Y. Liu, Y. Li, P. Yue, G. Cao, and Z. He, "An active-rectifier-based maximum efficiency tracking method using an additional measurement coil for wireless power transfer," *IEEE Trans. Power Electron.*, vol. 33, no. 1, pp. 716–728, Jan. 2018, doi: 10.1109/TPEL.2017.2665040.

[10] Y. Yao, P. Sun, X. Liu, Y. Wang, and D. Xu, "Simultaneous wireless power and data transfer: A comprehensive review," *IEEE Trans. Power Electron.*, vol. 37, no. 3, pp. 3650–3667, Mar. 2022, doi: 10.1109/TPEL.2021.3117854.

[11] A. Mulla, J. Baviskar, S. Khare, and F. Kazi, "The wireless technologies for smart grid communication: A review," in *Proc. 5th Int. Conf. Commun. Syst. Netw. Technol.*, 2015, pp. 442–447, doi: 10.1109/CSNT.2015.146.

[12] K. Strama, D. Weber, and H. Renkewitz, "Evaluation of Wifi data transmission algorithms for short distance underwater communication," in *Proc. OCEANS San Diego – Porto*, 2021, pp. 1–6, doi: 10.23919/OCEANS44145.2021.9705847.

[13] G. Simard, M. Sawan, and D. Massicotte, "High-speed OQPSK and efficient power transfer through inductive link for biomedical implants," *IEEE Trans. Biomed. Circuits Syst.*, vol. 4, no. 3, pp. 192–200, Jun. 2010, doi: 10.1109/TBCAS.2009.2039212.

[14] S. Atluri and M. Ghovanloo, "A wideband power-efficient inductive wireless link for implantable microelectronic devices using multiple carriers," in *Proc. IEEE Int. Symp. Circuits Syst.*, vol. 54, no. 10, Oct. 2007, pp. 2211–2221, doi: 10.1109/ISCAS.2006.1692789.

[15] A. Trigui et al., "Generic wireless power transfer and data communication system based on a novel modulation technique," *IEEE Trans. Circuits Syst. I, Reg. Papers*, vol. 67, no. 11, pp. 3978–3990, Nov. 2020, doi: 10.1109/TCSI.2020.3010308.

[16] C.-C. Huang and C.-L. Lin, "Wireless power and bidirectional data transfer scheme for battery charger," *IEEE Trans. Power Electron.*, vol. 33, no. 6, pp. 4679–4689, Jun. 2018, doi: 10.1109/TPEL.2017.2725940.

[17] Z. Yan, Z. Xiang, L. Wu, and B. Wang, "Study of wireless power and information transmission technology based on the triangular current waveform," *IEEE Trans. Power Electron.*, vol. 33, no. 2, pp. 1368–1377, Feb. 2018, doi: 10.1109/TPEL.2017.2678503.

[18] K. Divya, R. Maheswar, and P. Jayarajan, "Mitigation of interference in underwater wireless acoustic communication - A survey," in *Proc. Int. Conf. Commun. Signal Process.*, 2020, pp. 569–573, doi: 10.1109/ICCSP48568.2020.9182241.

[19] X. Li, C. Tang, X. Dai, P. Deng, and Y. Su, "An inductive and capacitive combined parallel transmission of power and data for wireless power transfer systems," *IEEE Trans. Power Electron.*, vol. 33, no. 6, pp. 4980–4991, Jun. 2018, doi: 10.1109/TPEL.2017.2725990.

[20] Y. Yao, Y. Wang, X. Liu, H. Cheng, M. Liu, and D. Xu, "Analysis, design, and implementation of a wireless power and data transmission system using capacitive coupling and double-sided LCC compensation topology," *IEEE Trans. Ind. Appl.*, vol. 55, no. 1, pp. 541–551, Jan./Feb. 2019, doi: 10.1109/TIA.2018.2869120.

[21] G. Wei, J. Feng, J. Zhang, C. Wang, C. Zhu, and S. Y Ostanin, "An efficient power and data synchronous transfer method for wireless power transfer system using double-D coupling coil," *IEEE Trans. Ind. Electron.*, vol. 68, no. 11, pp. 10643–10653, Nov. 2021, doi: 10.1109/TIE.2020.3038081.

[22] Y. Yao et al., "Analysis and design of a simultaneous wireless power and data transfer system featuring high data rate and signal-to-noise ratio," *IEEE Trans. Ind. Electron.*, vol. 68, no. 11, pp. 10761–10771, Nov. 2021, doi: 10.1109/TIE.2020.3031518.

[23] L. Ji, L. Wang, C. Liao, and S. Li, "Simultaneous wireless power and bidirectional information transmission with a single-coil, dual-resonant structure," *IEEE Trans. Ind. Electron.*, vol. 66, no. 5, pp. 4013–4022, May 2019, doi: 10.1109/TIE.2018.2831196.

[24] P. Wang, Y. Sun, Y. Feng, T. Feng, Y. Fan, and X. Li, "An improvement of SNR for simultaneous wireless power and data transfer system with full-duplex communication mode," *IEEE Trans. Power Electron.*, vol. 37, no. 2, pp. 2413–2424, Feb. 2022, doi: 10.1109/TPEL.2021.3106903.

[25] P. Wang, Y. Sun, T. Feng, Y. Fan, and Y. Feng, "Simultaneous wireless power and data transfer system with full-duplex mode based on double-side LCCL and dual-notch filter," *IEEE J. Emerg. Sel. Topics Power Electron.*, vol. 10, no. 3, pp. 3140–3151, Jun. 2022 doi: 10.1109/JESTPE.2021.3126337.

[26] Y. Fan, Y. Sun, X. Dai, Z. Zuo, and A. You, "Simultaneous wireless power transfer and full-duplex communication with a single coupling interface," *IEEE Trans. Power Electron.*, vol. 36, no. 6, pp. 6313–6322, Jun. 2021, doi: 10.1109/TPEL.2020.3035782.

[27] Y. Sun, P. -X. Yan, Z. -H. Wang, and Y. -Y. Luan, "The parallel transmission of power and data with the shared channel for an inductive power transfer system," *IEEE Trans. Power Electron.*, vol. 31, no. 8, pp. 5495–5502, Aug. 2016, doi: 10.1109/TPEL.2015.2497739.

[28] Y. Yao, H. Cheng, Y. Wang, J. Mai, K. Lu, and D. Xu, "An FDM-based simultaneous wireless power and data transfer system functioning with high-rate full-duplex communication," *IEEE Trans. Ind. Inf.*, vol. 16, no. 10, pp. 6370–6381, Oct. 2020, doi: 10.1109/TII.2020.2967023.

[29] Z. Qian, R. Yan, J. Wu, and X. He, "Full-duplex high-speed simultaneous communication technology for wireless EV charging," *IEEE Trans. Power Electron.*, vol. 34, no. 10, pp. 9369–9373, Oct. 2019, doi: 10.1109/TPEL.2019.2909303.

[30] S. Li, W. Li, J. Deng, T. D. Nguyen, and C. C. Mi, "A double-sided LCC compensation network and its tuning method for wireless power transfer," *IEEE Trans. Veh. Technol.*, vol. 64, no. 6, pp. 2261–2273, Jun. 2015, doi: 10.1109/TVT.2014.2347006.

[31] R. Mai, Y. Chen, Y. Li, Y. Zhang, G. Cao, and Z. He, "Inductive power transfer for massive electric bicycles charging based on hybrid topology switching with a single inverter," *IEEE Trans. Power Electron.*, vol. 32, no. 8, pp. 5897–5906, Aug. 2017, doi: 10.1109/TPEL.2017.2654360.

[32] B. Yang et al., "Analysis and design of a T/S compensated IPT system for AGV maintaining stable output current versus air gap and load variations," *IEEE Trans. Power Electron.*, vol. 37, no. 5, pp. 6217–6228, May 2022, doi: 10.1109/TPEL.2021.3135053.

[33] Y. Chen et al., "Variable-parameter T-circuit-based IPT system charging battery with constant current or constant voltage output," *IEEE Trans. Power Electron.*, vol. 35, no. 2, pp. 1672–1684, Feb. 2020, doi: 10.1109/TPEL.2019.2920948.

[34] D. W. Knight, "The self-resonance and self-capacitance of solenoid coils -applicable theory, models and calculation methods," May 2016. [Online]. Available: https://www.researchgate.net/publication/301824613_The_selfresonance_and_self-capacitance_of_solenoid_coils_applicable_theory_models_and_calculation_methods, doi: 10.13140/RG.2.1.1472.0887.

[35] J. Mai, Y. Wang, X. Zeng, Y. Yao, K. Wu, and D. Xu, "A multi-segment compensation method for improving power density of long-distance IPT system," *IEEE Trans. Ind. Electron.*, vol. 69, no. 12, pp. 12795–12806, Dec. 2022, doi: 10.1109/TIE.2021.3131800.

[36] Robert S. Elliott, "Electromagnetics in free space," in *Electromagnetics: History, Theory, and Applications*, 1st ed. New York, NY, USA: McGraw-Hill, 1993, pp. 309–314.

[37] A. Ayachit and M. K. Kazimierczuk, "Self-capacitance of single-layer inductors with separation between conductor turns," *IEEE Trans. Electromagn. Compat.*, vol. 59, no. 5, pp. 1642–1645, Oct. 2017, doi: 10.1109/TEMC.2017.2681578.

[38] C. Wu, H. Kim, S. Penugonda, and J. Fan, "Analysis and modeling of the common-mode conducted EMI from a wireless power transfer system for mobile applications," *IEEE Trans. Electromagn. Compat.*, vol. 63, no. 6, pp. 2143–2150, Dec. 2021, doi: 10.1109/TEMC.2021.3087700.

Yijie Wang (Senior Member, IEEE) was born in Heilongjiang Province, China, in 1982. He received the B.S., M.S., and Ph.D. degrees in electrical engineering from the Harbin Institute of Technology, Harbin, China, in 2005, 2007, and 2012, respectively.

From 2012 to 2014, he was a Lecturer with the Department of Electrical and Electronics Engineering, Harbin Institute of Technology. From 2014 to 2017, he was an Associate Professor with the Department of Electrical and Electronics Engineering, Harbin Institute of Technology. Since 2017, he has been a Professor with the Department of Electrical and Electronics Engineering, Harbin Institute of Technology. His research interests include dc–dc converters, soft-switching power converters, power factor correction circuits, digital control electronic ballasts, and LED lighting systems.

Prof. Wang is an Associate Editor of IEEE TRANSACTIONS ON INDUSTRIAL ELECTRONICS, IEEE JOURNAL OF EMERGING AND SELECTED TOPICS IN POWER ELECTRONICS, IEEE ACCESS, *IET Power Electronics,* and *Journal of Power Electronics*.

Tao Li (Graduate Student Member, IEEE) was born in Liaoning, China, in 1997. He received the B.S. and M.S. degrees in electrical engineering from the Dalian University of Technology (DUT), Dalian, China, in 2018 and 2021, respectively. He is currently working toward the Ph.D. degree in electrical engineering with the School of Electrical Engineering and Automation of Harbin Institute of Technology (HIT), Harbin, China.

His current research interests include wireless power transfer, magnetic coupler design, and simultaneous wireless power and data transfer.

Ming Zeng was born in Hunan, China, in 1999. He received the B.S. degree in electrical engineering, in 2021, from the Harbin Institute of Technology, Harbin, China, where he is working toward the M.S. degree.

His research interests include wireless power and data transfer and magnetic coupling structure design.

Jianwei Mai (Student Member, IEEE) was born in Henan, China, in 1994. He received the B.S. degree in electrical engineering, in 2017, from the Harbin Institute of Technology, Harbin, China, where he is working toward the Ph.D. degree.

His research interests include inductive power transfer and magnetic coupling structure design.

Peng Gu (Graduate Student Member, IEEE) was born in Harbin, Heilongjiang Province, China. He received the B.S. degree in electrical engineering from the Huazhong University of Science and Technology, Wuhan, China, in 2015, and the M.S. degree in electrical engineering from the China Electric Power Research Institute (CEPRI), Beijing, China, in 2018. He is currently working toward the Ph.D. degree in electrical engineering with the School of Electrical Engineering and Automation of Harbin Institute of Technology (HIT), Harbin, China.

His current research interests include wireless power transfer, magnetic coupling structure design, electromagnetic transient analysis, overvoltage and insulation coordination of EHV/UHV ac system, and dc–dc converter.

Dianguo Xu (Fellow, IEEE) received the B.S. degree in control engineering from the Harbin Engineering University, Harbin, China, in 1982, and the M.S. and Ph.D. degrees in electrical engineering from Harbin Institute of Technology (HIT), Harbin, China, in 1984 and 1989, respectively.

In 1984, he joined the Department of Electrical Engineering, HIT, as an Assistant Professor. Since 1994, he has been a Professor with the Department of Electrical Engineering, HIT. He was the Dean of School of Electrical Engineering and Automation, HIT, from 2000 to 2010. He was the vice president of HIT, from 2014 to 2020. He has authored/coauthored more than 600 technical papers. His research interests include renewable energy generation technology, power quality mitigation, sensorless vector-controlled motor drives, and high-performance servo system.

Prof. Xu is a Chairman of IEEE Harbin Section, Co-EIC of the IEEE TRANSACTIONS ON POWER ELECTRONICS, and an Associate Editor of the IEEE TRANSACTIONS ON INDUSTRIAL ELECTRONICS, and the IEEE JOURNAL OF EMERGING AND SELECTED TOPICS IN POWER ELECTRONICS. He was the recipient of the 2018 IEEE IAS Outstanding Achievement Award.